



1 **Smoke in the river: an AEROCLO-sA case study**

2 Cyrille Flamant¹, Marco Gaetani^{1,2,3}, Jean-Pierre Chaboureau⁴, Patrick Chazette⁵, Juan Cuesta², Stuart
3 J. Piketh⁶, and Paola Formenti²

4 ¹Laboratoire Atmosphère Milieux Observations Spatiales (LATMOS)/IPSL, UMR CNRS 8190, Sorbonne
5 Université, UVSQ, Paris, France

6 ²Université de Paris and Univ Paris Est Creteil, CNRS, LISA, F-75013 Paris, France

7 ³Scuola Universitaria Superiore IUSS, Pavia, Italy

8 ⁴Laboratoire d'Aérodynamique (LAERO), UMR CNRS 5560, Université de Toulouse, Toulouse, France

9 ⁵Laboratoire des Sciences du Climat et de l'Environnement (LSCE)/IPSL, UMR CNRS 1572, CEA, UVSQ,
10 Gif-sur-Yvette, France

11 ⁶School of Geo- and Spatial Science, North-West University, Potchefstroom, South Africa

12 Correspondence to: Cyrille Flamant (cyrille.flamant@latmos.ipsl.fr)

13

14 **Abstract**

15 The formation of a river of smoke crossing southern Africa is investigated during the Aerosols,
16 Radiation and Clouds in southern Africa (AEROCLO-sA) campaign in September 2017. A complementary
17 set of global and mesoscale numerical simulations as well as ground-based, airborne and space-borne
18 observations of the dynamics, thermodynamics and composition of the atmosphere are used to
19 characterize the river of smoke in terms of timing and vertical extent of the biomass burning aerosol
20 (BBA) layer.

21 The study area was under the synoptic influence of a coastal low rooted in a tropical easterly wave, a
22 high-pressure system over the continent and westerly waves in mid-latitudes, one of which had an
23 embedded cut-off low (CoL). The coastal low interacted with the second of two approaching westerly
24 waves and ultimately formed a mid-level temperate tropical trough (TTT). The TTT created the fast
25 moving air mass transported to the southwestern Indian Ocean as a river of smoke. The CoL, which
26 developed and intensified in the upper levels associated with the first (easternmost) westerly wave,
27 remained stationary above northern Namibia prior to the formation of the TTT and was responsible
28 for the thickening of the BBA layer.

29 This shows that the evolution of the river of smoke is very much tied to the evolution of the TTT while
30 its vertical extent is related to the presence of the CoL. The mechanisms by which the CoL, observed
31 over Namibia in the entrance region of the river of smoke, influences the vertical structure of the BBA
32 layer is mainly associated with the ascending motion above the BBA layer. In the presence of the CoL,
33 the top of the BBA layer over northern Namibia reaches altitudes above 8 km. This is much higher than
34 the average height of the top of the BBA layer over the regions where the smoke comes from (Angola,
35 Zambia, Zimbabwe, Mozambique) which is 5 to 6 km.

36 The results suggest that the interaction between the TTTs and the CoLs which form during the winter
37 may have a role in promoting the transport of BBA from fire-prone regions in the tropical band to the
38 temperate mid-latitudes and southwestern Indian Ocean.

39

40 **Key words:** Biomass burning aerosols; southern Africa fires; cut-off low; tropical temperate trough;
41 planetary boundary layer; Meso-NH; ERA5; CAMS; airborne lidar; CATS; MODIS; AERONET

42



43 1. Introduction

44 Widespread, coherent bands of smoke from forest fires are regularly observed to cross the southern
45 African sub-continent near the end of southern Africa's dry season, and particularly in September
46 (Annegarn et al., 2002; McMillan et al., 2003; Swap et al., 2003). These features are generally referred
47 to as 'rivers of smoke' (owing to the sharply defined boundaries of the smoke plume, giving them the
48 appearance of a 'river') and can be several hundred kilometres wide and extend over a few thousands
49 kilometres while flowing off the southeast coast of Africa. The smoke transported in these rivers is
50 coming from thousands of agricultural fires as well as accidental forest fires burning in Angola, Zambia,
51 Zimbabwe, Mozambique, the Democratic Republic of Congo and South Africa, favoured by dry
52 conditions during the austral winter (see Figure 1 in Roberts et al., 2009). The smoke from the southern
53 African sub-continent is generally contained in multiple stratified layers trapped below approximately
54 850hPa, 700hPa and 500hPa, depending on synoptic conditions (Stein et al., 2003). The river-of-smoke
55 events generally correspond to the direct eastward transport of biomass burning aerosols (BBA) from
56 southern Africa to the southwest Indian Ocean in five main transport paths classified by Garstang et
57 al. (1996). These trajectories lead to the transport of massive amounts of aerosols and gases (e.g.
58 carbon monoxide) towards the southwest Indian Ocean (Dufлот et al., 2010) and as far as southeast
59 Australia (Pak et al., 2003; Sinha et al., 2004), with potential important implications for the radiative
60 budget and the marine productivity of the region (Luo et al., 2008).

61 The aerosol properties, transport and distribution across southern Africa, the South Atlantic and the
62 Indian Ocean have been widely investigated for their key role in controlling the radiative budget in the
63 region and, consequently, global climate dynamics (Zuidema et al. 2016a, b; Haywood et al. 2021;
64 Redemann et al. 2021). Recently, the long term aerosol transport in the region has been characterised
65 in terms of synoptic weather patterns (Gaetani et al., 2021). Nevertheless, to date, the rivers of smoke
66 have exclusively been studied in the framework of the 2000 Southern African Regional Science
67 Initiative (SAFARI 2000) using ground-based, airborne and space-borne observations (Annegarn et al.,
68 2002; Jury and Freiman, 2002; Swap et al., 2003; McMillan et al., 2003; Stein et al., 2003; Schmid et al.,
69 2003; Pak et al., 2003; Magi et al., 2004) as well as numerical simulations (Sinha et al., 2004). Among
70 other studies, Stein et al. (2003) have shown that they form in regions where high-pressure and low-
71 pressure synoptic-scale systems are juxtaposed to constrain the shape of the aerosol rivers.

72 Rivers of smoke are very effective at transporting large amounts of smoke from the fire-prone tropical
73 regions into the mid-latitude westerly circulation (Annegarn et al., 2002). Surface synoptic conditions
74 in the tropical zone are generally dominated by easterly waves and associated lows, whereas aloft a
75 more stable anticyclonic circulation prevails in association with the continental high pressure system.
76 The subtropical latitudes are dominated by continental highs and baroclinic westerly waves at all levels
77 (Jury and Freiman, 2002). Hence, the transport of smoke from the Tropical Africa to the southwest
78 Indian Ocean implies the formation of complex synoptic systems that can bridge two climatic regions,
79 namely the tropical band (10–20°S) and the temperate subtropical band (20–30°S) over the southern
80 Africa sub-continent.

81 Tropical temperate troughs (TTTs) are generally described as an interaction between tropical
82 convection and mid-latitude transient perturbations (see Todd et al. 2004 and references therein) and
83 typically form when a tropical disturbance in the lower atmosphere is coupled with a mid-latitude
84 trough in the upper atmosphere (Lyons, 1991). Mid-latitude baroclinic waves are a necessary condition
85 for TTT development (Macron et al., 2014). TTTs are known to be the dominant rainfall-producing
86 weather system over southern Africa during the austral summer, when they form a cloud band that
87 extends along the northwest-southeast direction across the landmass and the adjacent southwest
88 Indian Ocean (Ratna et al., 2013; Howard et al., 2019; and references therein) and tend to propagate
89 eastward. TTT events have been suggested to act as a major mechanism of poleward transfer of
90 moisture owing to the strong convergence forming a pronounced poleward flux along the cloud band
91 (Ratna et al., 2013). However, the role of TTTs in the transport of BBA during the winter has never been
92 investigated until now.



93 During the AEROCLO-sA (AErosol, RadiatiOn and CLOuds in southern Africa) field campaign held in
94 Namibia in August-September 2017 (Formenti et al., 2019), a river of smoke was observed to sweep
95 through southern Africa from west to east, between 5 and 6 September 2017. The study area was
96 under the synoptic influence of a coastal low rooted in a tropical easterly wave, a high-pressure system
97 over the continent and westerly waves in the mid-latitudes, one of which had an embedded cut-off
98 low (CoL; Favre et al., 2012). During this period, the coastal low interacted with the second of two
99 approaching westerly waves and ultimately formed a mid-level TTT, which created the fast moving
100 limb of air transported to the southwest Indian Ocean as a river of smoke. The CoL, that developed
101 and intensified in the upper levels associated with the first (easternmost) of the two approaching
102 westerly waves, remained stationary above northern Namibia prior to the formation of the TTT (from
103 2 to 4 September 2017) and was responsible for the thickening of the BBA layer that subsequently was
104 conveyed southeastward. The objective of the paper is to assess the respective impact of both the CoL
105 and the TTT on the atmospheric circulation and composition in the mid- and lower troposphere over
106 southern Africa prior to and during the river of smoke event.

107 In Section 2 we present the model simulations and measurements used in the study. In Section 3, we
108 detail the life cycle of the CoL and the TTL over Western Namibia, while their impact on the formation
109 of the river of smoke event over southern Africa are analysed in Section 4. We also detail the vertical
110 distribution and origin of smoke in the lower troposphere over northern Namibia, in the entrance
111 region of the river of smoke, using airborne measurements made on 5 and 6 September. In Section 5,
112 the impact of the CoL and the TTT on the tropospheric composition over the sub-continent is
113 investigated. Finally, we summarize and conclude in Section 6.

114

115 2. Data

116 2.1 Modelling

117 2.1.1 ECMWF reanalysis products: ERA5 and CAMS

118 The regional circulation over continental southern Africa and adjacent oceans for the period 1 – 6
119 September 2017 is analysed using ERA 5 reanalysis (Fifth European Centre for Medium-range Weather
120 Forecast Reanalysis; Hersbach et al. 2018). The reanalysis outputs are available every hour on a 0.25°
121 $\times 0.25^\circ$ grid, as well as 137 pressure levels, 88 of which are below 20 km and 60 below 5 km (note that
122 only 37 levels are available for download). Among the available variables, we focus on mean sea level
123 pressure (MSLP), geopotential height (Z), potential vorticity (PV), outgoing longwave radiation (OLR),
124 vertical velocity (ω) and wind.

125 We also make use of the Copernicus Atmospheric Monitoring Service (CAMS; Inness et al., 2019)
126 reanalysis available every 3 hours (00, 03, 06, 09, 12, 15, 18 and 21 UTC) with a resolution of
127 approximately 80 km and 60 pressure levels (37 of which are below 20 km and 20 below 5 km), to
128 analyse the evolution of BBA during the episode of interest (note that only 25 levels are available for
129 download). For consistency with ERA5 data, CAMS data have been interpolated onto a 0.25° regular
130 grid. In the following, we use organic matter as a proxy for BBA. In addition, we have compared to
131 same dynamical and thermodynamic variables as for ERA5 in order to check the consistency between
132 the two types of products. This is essential as we intend to investigate the relationship between the
133 atmospheric dynamics and the distribution of BBA. It turns out that fields such as PV, ω , wind, relative
134 humidity are very consistent between ERA5 and CAMS (not shown).

135 The evolution of the BBA transport and the associated atmospheric circulation from 1 to 6 September
136 2017 above Namibia is analysed by using a principal component analysis (PCA) of organic matter
137 aerosol optical thickness (AOT) at 550 nm, MSLP and Z at 700 and 300 hPa from the CAMS reanalysis
138 product. PCA consists in projecting data variability onto an orthogonal basis by solving the eigenvalue
139 problem of the data covariance matrix, so that data variability is decomposed into independent
140 variability modes, each explaining a fraction of the total variability (von Storch and Zwiers, 1999). Each



141 variability mode is presented as an empirical orthogonal function (EOF), accounting for the anomaly
142 pattern of the variable related to the mean of the analysed period, and the associated PC time series
143 accounting for the evolution of the anomaly amplitude. It follows that negative values indicate a
144 reversal of the anomaly pattern.

145 2.1.2 *Meso-NH*

146 A high-resolution simulation of the atmospheric dynamics, thermodynamics and composition for the
147 case study was also run with the non-hydrostatic mesoscale model Meso-NH (Lac et al. 2018), version
148 5.4, over a domain covering southern Africa. The model was run on a grid with 5-km horizontal spacing
149 and 64 levels with a resolution of 60 m close to the surface to 600 m at high altitude. It was run for 6
150 days starting from 000 UTC on 1 September 2017. The lateral boundary conditions were given by
151 ECMWF operational analysis. The simulation used the Surface Externalisée (SURFEX) scheme for
152 surface fluxes (Masson et al. 2013), a 1.5-order closure scheme for turbulence (Cuxart et al. 2000), an
153 eddy-diffusivity mass-flux scheme for shallow convection (Pergaud et al. 2009), a microphysical
154 scheme for mixed-phase clouds (Pinty and Jabouille 1998), a statistical scheme for subgrid cloud cover
155 (Chaboureaud and Bechtold 2002), the Rapid Radiative Transfer Model (Mlawer et al. 1997) for
156 longwave radiation and the two-stream scheme (Fouquart and Bonnel 1986) for shortwave radiation.
157 Emission, transport and deposition of dust were parameterized using a prognostic scheme (Grini et al.
158 2006) to allow online interaction with radiation. A black carbon passive tracer was emitted following
159 the daily Global Fire Emissions Database (GFED) version 4, available at a horizontal resolution of
160 $0.25^\circ \times 0.25^\circ$ (van der Werf et al. 2017). Backward trajectories were computed using three passive
161 tracers initialized with the 3D coordinates of each grid cell at their initial location (Gheusi and Stein
162 2002). A mass extinction efficiency of $5.05 \text{ m}^2 \text{ g}^{-1}$ (representative of aged smoke as in Mallet et al.,
163 2019) was used to compute AOT at 550 nm from black carbon concentration simulated by Meso-NH.

164 2.2 Observations

165 2.2.1 *Ground-based observations*

166 The National Aeronautics and Space Administration Aerosol Robotic Network (NASA AERONET)
167 operates a number of sun spectral photometers in Namibia and South Africa, providing long-term and
168 continuous monitoring of aerosol optical, microphysical and radiative properties. We use level-2.0
169 (cloud-screened and quality-assured) AOT at 500 nm data. AERONET stations of interest are located in
170 Windpoort, Bonanza, the HESS (High Energy Stereoscopic System) site and Henties Bay (Namibia) as
171 well as Upington (South Africa), (see **Figure 1**).

172 2.2.2 *Airborne observations*

173 For the period from 5 to 12 September 2017, dynamics and thermodynamics profiles over continental
174 Namibia were obtained from dropsondes released from a high-flying aircraft, the French Falcon 20
175 aircraft for environmental research of Safire (Service des Avions Français Instrumentés pour la
176 Recherche en Environnement) based in Walvis Bay, on the west coast of Namibia (see **Figure 1**). The
177 vertical structure of the aerosol layers was obtained from the nadir-pointing airborne lidar LEANDRE
178 Nouvelle Génération (LNG; Bruneau et al., 2015) installed on the same aircraft. Details about the Safire
179 Falcon 20 flights, the lidar LNG and the dropsonde launching unit can be found in Formenti et al. (2019).
180 In the following we shall only analyse lidar and dropsonde data acquired on 5 and 6 September 2017.

181 On 5 September, the Falcon 20 circuit from and to Walvis Bay was performed counter clockwise from
182 0736 to 1014 UTC (flight F06). On 6 September, the Falcon 20 circuit was performed clockwise from
183 1055 to 1401 UTC (flight F09). On both flights, the aircraft flew around 10 km above mean sea level
184 (AMSL), except on 6 September between 1145 and 1218 UTC when the aircraft performed a sounding
185 and penetrated the BBA layer over the Etosha pan. In the following, we will discuss the dynamics and
186 thermodynamics profiles from 2 dropsondes released over the Etosha pan at nearly the same location:
187 $16.445^\circ \text{E} / 18.772^\circ \text{S}$ on 5 September at 0839 UTC and $16.401^\circ \text{E} / 18.766^\circ \text{S}$ on 6 September at 1146
188 UTC. We also compare these profiles to the one obtained in the vicinity of Henties Bay, over the ocean



189 at 13.78°E / 21.69°S on 5 September at 0951 UTC, and to those obtained south of Etosha at 16.33°E /
190 21.74°S on 6 September at 1137 UTC. Note that the drosponde data acquired during AEROCLO-sA have
191 not been assimilated in the ECMWF operational analysis nor in the reanalysis.

192 The signal backscattered to the LNG system telescope at 1064 nm is range-square-corrected to
193 produce atmospheric reflectivity. Total attenuated backscatter coefficient (ABC) profiles are derived
194 from atmospheric reflectivity profiles by normalizing the atmospheric reflectivity above the aerosol
195 layers to the molecular backscatter coefficient profiles. Hence the slope of the lidar reflectivity above
196 7.5 km AMSL matched that of the molecular backscatter derived from dropsonde measurements of
197 pressure and temperature. In the following, we only use ABC at 1064 nm because the attenuation by
198 the BBA in the lower troposphere, in spite of being important, does not prevent the lidar signal from
199 reaching the surface, unlike at the other wavelengths of operation of LNG (i.e. 355 and 532 nm). The
200 vertical resolution of the ABC profiles is 30 m. Profiles are averaged over 5 s, yielding a horizontal
201 resolution of 1 km for an aircraft flying at 200 m s⁻¹ on average. It is worth noting that ABC as observed
202 with LNG is sensitive to both aerosol concentration and aerosol hygroscopicity. Indeed, relative (RH)
203 in excess of 60% modify the size and the complex refractive index of aerosol, and hence their optical
204 properties, enhancing the ABC (e.g. Randriamiarisoa et al., 2006).

205 2.2.3 Space-borne observations

206 We make use AOT (at 550 nm) and fire hot-spot locations from the National Aeronautics and Space
207 Administration Moderate Resolution Imaging Spectroradiometer (NASA MODIS; King et al., 1992). We
208 also make use of ABC and aerosol typing products obtained from the space-borne Cloud-Aerosol
209 Transport System (CATS; Yorks et al., 2016) to gather information on the vertical structure of aerosol
210 and cloud layers as well as aerosol composition over Namibia from two overpasses on 4 and 5
211 September 2017. Details about the space-borne products used in this study can be found in Chazette
212 et al. (2019). The horizontal distribution of the smoke plumes is also described daily with total column
213 amounts of carbon monoxide (CO) derived from radiance spectra measured by the Infrared
214 Atmospheric Sounding Spectrometer (IASI; Clerbaux et al., 2009), on-board the MetOp-A and MetOp-
215 B satellites and overpassing the region around 0830 and 0900 LT (local time) respectively. This satellite
216 dataset is retrieved using the Fast Optimal Retrievals on Layers for IASI algorithm (Hurtmans et al.,
217 2012) and validated against airborne and space-borne observations (Georges et al., 2009; De Watcher
218 et al., 2012). Finally, we utilize RGB natural colour imagery of cloud cover obtained with the Spinning
219 Enhanced Visible and InfraRed Imager (SEVIRI) instrument on-board the geostationary satellite
220 MeteoSat Second Generation.

221

222 3. Synoptic conditions over southern Africa: a tale of two features

223 3.1 The life cycle of the CoL and the TTT

224 In the low levels, the northern part of Namibia is under the influence of easterly flow, and on 1
225 September a marked coastal trough is seen along the west coast of Namibia, west of the instrumented
226 sites, associated with an easterly wave (**Figure 2a**). In the following days (2-3 September), a weak
227 coastal trough is seen to develop offshore (**Figure 2b,c**). Further south, a belt of high pressure systems
228 is present in the vicinity of the tip of the southern Africa sub-continent (e.g. **Figure 2a-c**). From 4
229 September, as the baroclinic westerly flow approaches the west coast, a distinct low forms over Angola
230 and northern Namibia within the easterly flow (**Figure 2d-f**), which corresponds to the Angola low in
231 the mid-troposphere. During the same period, the Southeast Atlantic high pressure system (St Helena
232 anticyclone) is strengthening (**Figure 2d**). Its eastern fringe is approaching the land on 5 September
233 (**Figure 2e**) and even intrudes over the sub-continent on 6 September (**Figure 2f**).

234 **Figure 3** shows the evolution of the ERA5 geopotential and potential velocity (PV) at 300 hPa at 1200
235 UTC over the area of interest. On 1 September, the instrumented sites over northern Namibia are
236 under the influence of a westerly flow in the upper levels, which is clearly separated from the main



237 westerlies located poleward of 40°S (**Figure 3a**). The split in the westerlies is generally associated with
238 the breaking of the upper level jet and seen upstream of southern Africa at 10°W (Favre et al., 2012).
239 Strong negative PV is associated with the cyclonic circulation in the area of separation between the
240 main westerlies and the northern westerlies branch, just west of the Namibian coastline. On 2
241 September, the region of splitting reaches the coastline, and some of the instrumented sites in the
242 southern part of the domain and along the coast are under the influence of a southerly flow, while the
243 sites to the north are under a westerly flow (**Figure 3b**). The maximum of negative PV is located
244 approximately above the AERONET HESS site. The main westerly flow exhibits a pronounced poleward
245 dip just west of the tip of South Africa which is further enhanced on the following day, when the closed
246 circulation has formed and is centred over the region of the AERONET Bonanza site (**Figure 3c**). This
247 closed circulation now contains the strongest negative PV feature. In the ERA5 reanalysis, ascending
248 motion is present to the north and east of the CoL centre, while descending motion is highlighted to
249 the south and west of the CoL centre (**Figure S1a**). The CoL is positioned in the same area the next day
250 (4 September, **Figure 3d**), with the instrumented sites being essentially beneath the negative PV
251 associated with the CoL. On this day also, ascending motion is present to the north and east of the CoL
252 centre, while descending motion is highlighted to the south and west of the CoL centre (**Figure S1b**).
253 The CoL starts deforming shortly after and becomes elongated in the north-south direction, and can
254 be seen as an elongated filament of negative PV to the east of most of the instrumented sites located
255 in Namibia. It is then moving poleward and merges back with the main westerly flow between 0900
256 and 1200 UTC on 5 September (not shown). The area of interest lies below a hump in the north-
257 westerly flow on the eastern side of the poleward dip of the westerlies (**Figure 3e**). Finally, on 6
258 September, the area of interest is under a rather weak east-northeasterly flow, north of the main
259 westerlies located south of 40°S (**Figure 3f**). The filament of negative PV marking the remains of the
260 CoL has now moved further southeast over South Africa and over the Indian Ocean.

261 On 3 September, the CAMS-derived circulation at 700 hPa shows, equatorward of the strong
262 westerlies, the presence of a high pressure system over the southern tip of the continent as well as an
263 isolated low pressure feature (connected with the CoL) located offshore of Namibia, over the Atlantic
264 Ocean (**Figure 4a**). The cyclonic and anticyclonic circulations associated with the CoL and the high
265 pressure, respectively, create conditions that are favourable to the advection of BBA poleward,
266 between them as shown by Chazette et al. (2019). It is worth noting that at this level, both the low and
267 high pressure features are characterised by low BBA-related AOT. As the wave in the westerly flow at
268 700 hPa approaches the west coast of southern Africa on 4 September, the high pressure moves
269 eastward and is partly over the Indian Ocean (**Figure 4b**). At the same time, the low pressure becomes
270 elongated and is oriented almost parallel to the coastline (a shape that resembles that observed at 300
271 hPa on 4 September, see **Figure 3c**). The poleward advection of BBA at 700 hPa becomes more
272 pronounced and results in the formation of the river of smoke. On 5 September (**Figure 4c**), the
273 equatorward dip of the westerly flow is now positioned over southern Africa and the high pressure has
274 moved over the Indian Ocean (~20°W), generating a TTT aligned with the Namibian coast. The resulting
275 circulation promotes the poleward advection of a more massive river of smoke extending over the
276 eastern coast of southern Africa and over the Indian Ocean, and extends poleward almost to 50°S. The
277 signature of the CoL at 700 hPa is no longer identifiable. BBA over the Atlantic Ocean related to biomass
278 burning events over South America are also observed by Chazette et al. (2019). Finally, on 6 September,
279 the St Helena anticyclone pushes the poleward dip of the westerlies and the TTT further east, while
280 the high pressure system over the Indian Ocean also weakens (**Figure 4d**). The river of smoke is now
281 well established over southern Africa, and located further east, particularly over South Africa.

282 3.2 Dynamical controls

283 The variability of the BBA distribution in the period 1-6 September is compared with the atmospheric
284 circulation variability by means of a PCA. The first EOF of the organic matter AOT (**Figure 5a**), explaining
285 55% of the variability, shows a negative anomaly in the BBA transport until 4 September and a river of
286 smoke developing over Namibia on 5 and 6 September (red line in **Figure 5e**). BBA are mainly



287 transported at 700 hPa, and the evolution of the river of smoke is controlled by the circulation at this
288 level. The first EOF of the geopotential at 700 hPa (**Figure 5c**), explaining 74% of the variability at this
289 level, shows on 1-2 September a positive gradient along the northeast-southwest direction, which
290 drives a southeasterly flow inhibiting the northerly BBA transport. The gradient reverses on 4
291 September (green line in **Figure 5e**), favouring the southward penetration of the river of smoke. The
292 control on the BBA exerted by the circulation at 700 hPa is confirmed by the high correlation (0.78,
293 **Table 1**) of PCA time series in **Figure 5e**. The first EOF of the geopotential at 300 hPa (**Figure 5b**),
294 explaining 56% of the variability, shows the transit of the CoL along the meridional direction, migrating
295 from southern Namibia on 1 September to central Namibia on 3-4 September and retreating to the
296 south on 5-6 September (blue line in **Figure 5e**). The evolution of the AOT and geopotential PCAs
297 suggests a possible control of the river of smoke by the CoL from 4 September onwards (PCA
298 correlation is 0.50, **Table 1**), when high-low pressure dipole (**Figure 5b**) favours the channelling of the
299 BBA along the Namibian coast. The first EOF of the MSLP (**Figure 5d**), explaining 43% of the variability,
300 shows a coastal trough on 1-2 September evolving into a coastal ridge on 3-4 September (black line in
301 **Figure 5e**). The associated northwesterly flow could have a role in favouring the installation of the river
302 of smoke. However, the comparison of the PCAs (**Table 1**) shows no stable relationship between the
303 conditions at the surface and the BBA transport. In conclusion, the CoL, and the circulation at 300 hPa,
304 has a dominating influence on the circulation around 700 hPa (~4 km AMSL) and consequently on the
305 tropospheric composition over Namibia, as the circulation at this level controls the distribution of BBA
306 away from the main sources.

307

308 4. Smoke and clouds over southern Africa

309 4.1 The river of smoke in satellite and ground based observations

310 The position of the river of smoke in the CAMS reanalysis at 1200 UTC in **Figure 4b-d** matches the
311 observations retrieved from MODIS (**Figure 6**) and IASI (**Figure S2**), respectively in terms of AOT and
312 CO total amounts, on 4, 5 and 6 September. In particular, we remark the southward progression of the
313 plume between 4 and 5 September (**Figures 6a,c and S2b,c**) and then its eastward displacement
314 reaching the continent on 6 September (**Figures 6c, e and S2c,d**). For the AOT measurements, the
315 signature of the river of smoke is more distinct on 6 September over the continent (**Figure 6e**), thanks
316 to the mostly cloud-free conditions over southern Africa on that day. On the other hand, the river of
317 smoke on 5 September is more difficult to detect with the MODIS observations (**Figure 6c**), due to its
318 co-location with a band of mid-level clouds positioned along the Namibian coastline. CO retrievals
319 depicts the river of smoke both on 5 and 6 September (**Figure S2c,d**), as these measurements can also
320 be retrieved above low and mid-level relatively thin clouds. On 3-4 September, enhanced CO amounts
321 (adjacent to clouds, shown as blanks in the figure) already show an elongated plume over the Atlantic
322 extending from northwest to southeast over the latitude band 10-40°S, that probably corresponds to
323 the river of smoke transported eastwards over the continent and enhanced in concentration on the
324 two following days. This plume structure is simulated by CAMS reanalysis for BBA, but only extending
325 southwards to 30°S. After 5 September, the CO distributions also depicts the plume originating from
326 South America, located over the Atlantic (at 25-35°S, **Figure S2c, d**). This plume presents similar CO
327 amounts as that of the river of smoke ($3\text{-}3.5 \cdot 10^{18}$ molecules cm^{-2}) and it is transported eastwards until
328 reaching the western South African coast on 6 September (Chazette et al., 2019). This is qualitatively
329 consistent with the BBA plume shown by CAMS reanalysis, but these last ones show a relatively less
330 dense plume as compared to that of the river of smoke.

331 On 5 September, the space-borne lidar CATS overpassed southern Namibia at around 2200 UTC across
332 the mid-level cloud band (**Figure 7a**), just to the south of the Bonanza AERONET station (**Figure 6c**).
333 CATS provides further observational evidence that BBA dominate the aerosol composition of the low
334 troposphere over continental southern Africa during the period of interest (**Figure 7b**). Smoke is seen
335 to be well mixed over the depth of the boundary layer (~3 km) over northern Botswana and Zambia



336 where fires are observed to be very active and widespread (**Figure 6d**). Interestingly, the depth of the
337 smoke layer is seen to be much deeper over continental Namibia, its top reaching almost 7.5 km AMSL
338 in the vicinity of the mid-level cloud band. The smoke is observed to reach the coastline above 3 km
339 AMSL, consistently with MODIS observations. At lower altitude, CATS evidences the presence of
340 pollution at the coast and maritime aerosols further west of the ocean (**Figure 7b**).

341 The river of smoke is anchored over Angola and northern Namibia, the latter location being where
342 most airborne and ground-based observations were acquired in the course of the AEROCLO-sA
343 campaign. While the CATS observations suggest that further south the BBA layer is advected eastward,
344 it appears from the CAMS reanalysis and MODIS observations that the region where BBA feeds into
345 the river of smoke does not move significantly. This is confirmed by the fact that large AOTs are
346 observed over northern Namibia (AERONET sun-photometer station in Windpoort, **Figure 8a**) between
347 3 and 7 September, as opposed to the other AERONET stations further south (Bonanza, HESS,
348 Uptington, **Figure 8b,c,d**) where more sporadic AOT peaks are observed, suggesting a propagating BBA
349 feature over this area. Large BBA-related AOT values are seen with CAMS in the vicinity of the Etosha
350 pan region (**Figure 4c,d**) that correspond to the maximum in AOT seen with AERONET over the station
351 of Windpoort (**Figure 8a**). The aerosol load is seen to increase over Windpoort from 1 to 6 September
352 (when it reaches 1.75 at 500 nm) and to decrease thereafter. The AOT values in Windpoort are
353 systematically higher than AOTs derived from other AERONET stations further south. The timing of the
354 AOT peaks obtained with CAMS is consistent with its sun-photometer-derived counterpart. The AOT
355 peak in the CAMS reanalysis suggests that the smoke river overpassed the HESS site around 1200 UTC
356 on 5 September, the Uptington site at 0000 UTC on 6 September and the Bonanza site at 1800 UTC on
357 the same day, suggesting an eastward drift of the smoke river. The data from the AERONET sites is
358 consistent with the MODIS data in both magnitude and timing of the increased AOT values (**Figure**
359 **6c,e**). The river of smoke is clearly observed as an identifiable isolated feature sweeping through
360 Uptington, i.e. away from the fire emissions, as opposed to what is observed further north in Windpoort
361 which is closer to Angola and Zambia. The good agreement between the AOT from MODIS and CAMS
362 at Windpoort and Bonanza (**Figure 8a, b**) is expected as MODIS AOTs are assimilated in CAMS retrieval
363 algorithm. Good agreement is also found between CAMS and AERONET AOTs at Uptington (**Figure 8d**),
364 and to a lesser extent at HESS and Bonanza (**Figure 8b,c**, especially before 6 September). Windpoort
365 (**Figure 8a**) is an exception with AERONET AOTs differing significantly at times from the MODIS and
366 CAMS retrievals. The higher sun-photometer AOTs are most likely to be BBA dominated, a fact that is
367 highlighted by the average Angstrom coefficient values derived from the AERONET observations in
368 Windpoort of 1.7 (between 440 and 870 nm) which is consistent with previous finding evidencing that
369 the absorption Angstrom exponent of biomass smoke is typically between 1.5 and 2 (e.g. Bergstrom et
370 al., 2007).

371 4.2 Airborne observations and model simulation

372 In the latter stage of the CoL intrusion over Namibia (5 and 6 September), a large scale mid-level cloud
373 band is visible along the southern Africa western coastline at 0900 UTC on 5 September as already
374 highlighted using MODIS (**Figure 6c**) and confirmed using SEVIRI (**Figure S3a**), i.e. around the time the
375 Falcon 20 aircraft flew on that day. The presence of this cloud band is related with the presence of the
376 TTT (Ratna et al., 2013) and is triggered by the arrival of an upper-level trough over southern Africa
377 associated with the band of divergence east of its leading edge. Nearly cloud-free conditions are
378 observed over northern continental Namibia at this time. The mid-level cloud band moved inland
379 rapidly, together with the river of smoke, and covered a large part of Namibia in the afternoon as
380 shown with SEVIRI at 1600 UTC (**Figure S3b**). It sweeps through Namibia overnight and is observed
381 over eastern Namibia at 0600UTC on 6 September (**Figure S3c**) before starting to disintegrate. Almost
382 cloud-free conditions are seen after 1200 UTC (the cloud band is no longer visible in **Figure S3d**), at the
383 time of the Falcon 20 aircraft flight on that day. On 5 September, airborne observations acquired in
384 the morning are representative of conditions ahead of the cloud band sweeping across Namibia, while



385 the airborne data acquired in the afternoon of 6 September were acquired over Namibia after its
386 passage.

387 The observations made with the airborne lidar LNG over Windpoort and the Etosha region on 5 and 6
388 September (**Figure 9a, c**, respectively) clearly evidence the complexity of the layering within the BBA-
389 laden air masses. On the morning of 5 September the BBA layer is observed between ~ 2 and 6 km
390 AMSL and to be separated from the surface (reaching an elevation of 1.5 km AMSL over the plateau)
391 by a shallow developing convective boundary layer in which dust emission from the Etosha pan are
392 observed (Formenti et al., 2019). On the other hand, the BBA layer is separated from the surface away
393 from the plateau and over the ocean (beginning and end of flight). On the afternoon of 6 September,
394 the BBA layer is clearly observed to be mixed all the way down to the surface over the plateau and to
395 reach ~ 6 km AMSL, thereby extending over a depth of nearly 4.5 km. The vertical structure of the
396 Meso-NH-derived black carbon tracer along the flight tracks on both days is given in **Figure 9b, d**. On
397 5 September, the greater vertical extent of the BBA layer over the continental plateau (with respect to
398 the surrounding lower lands and ocean) at the beginning and the end of the flight is well captured in
399 the model (**Figure 9b**). Likewise, the decrease of the BBA layer over the sloping terrain towards the
400 ocean at the end of the flight on 6 September is also well represented (**Figure 9d**). On 6 September,
401 large concentrations of black carbon tracers are mixed all the way to the surface, as in the
402 observations, in the northern part of the flight (i.e. overpassing the Etosha pan). In contrast, the larger
403 black carbon tracer concentrations do not reach the surface in the morning, which was also observed
404 with the airborne lidar.

405 4.3 Analysis of BBA transport on 5 September

406 Meso-NH-derived backward trajectories ending at 0900 UTC 5 September 2017 along the F06 flight
407 track and at altitude between 1 and 5 km AMSL (**Figure 10a, c, d**) show that over the previous 3 days
408 the air masses documented with the airborne lidar LNG during the flight had travelled over regions
409 with detectable active fires (Figure 5) and where black carbon emissions are high in the GFED4s
410 inventory (**Figure S4**). The trajectories are transport emissions from Angola, Zambia, Zimbabwe and
411 Mozambique where fires are identified with MODIS (**Figure 6**). Airborne observations and simulations
412 show unambiguously that the atmospheric composition below 5 km AMSL along the aircraft flight track
413 is dominated by BBA from Angola and Mozambique (see **Figure 6**) coming from altitudes below 5 km
414 AMSL and swirling anticyclonically around a high pressure in the lower troposphere (**Figure 10**). It is
415 worth noting that the air masses ending at 4-5 km AMSL along the aircraft track all experience upgliding
416 in the previous 24 h (**Figure S5a**) while the black carbon tracer concentration is gradually increasing
417 over the 3 days for all air masses below 5 km AMSL (**Figure S5b**). At higher altitudes (i.e. 6-7 km AMSL),
418 backward trajectories ending north of the Etosha pan also start from Angola and Zambia below 5 km
419 AMSL (**Figure 10b**) while those ending south of the Etosha pan originate from higher altitudes
420 (between 8 and 11 km AMSL) and from the southeast, having travelled over Botswana, Mozambique
421 and South Africa, and to swirl cyclonically around the location of the CoL while descending along its
422 poleward fringes (recall that the CoL is located between Henties Bay, Bonanza and Windpoort on 3-4
423 September (**Figure 3c, d**)). The downgliding experienced by the air masses occurs in the previous 2
424 days (**Figure S4b**). The ERA5 data show the presence of ascending motion to the north and east of the
425 CoL centre and descending motion to the south and west of the CoL centre (see Section 3).

426 Airborne lidar observations evidence that over the ocean, the height of the cumulus clouds is observed
427 to coincide with the top of the BBA layer (**Figure 9a**). The dropsonde-derived RH and potential
428 temperature profiles acquired over the ocean (**Figure 11a**) show the presence of a strong RH and
429 temperature inversion at 6 km AMSL, topped by extremely dry air layer from the west (270°),
430 consistent with the backward trajectories seen in the southern part of the F06 flight track (**Figure 10b**).
431 This suggests a descent of upper tropospheric air along the southern fringes of the CoL. Directional
432 wind shear is observed in the BBA layer with northerly winds at the bottom (~ 2 km AMSL) and north-
433 northwesterly winds near the top (~ 6 km AMSL, **Figure 11b**), with the BBA layer being advected
434 towards the ocean at the speed of ~ 15 m s^{-1} . Over the Etosha pan, dry upper tropospheric air is



435 observed above 7 km AMSL, with significant RH above 6 km AMSL (**Figure 11c**). This, together with the
436 lidar-derived ABC observations, suggests that the BBA layer top can reach to almost 7 km AMSL
437 (enhanced ABC is observed above 6 km AMSL, i.e. above isolated cumulus-type clouds forming over
438 land). The wind direction in the air mass encompassing the upper part of the BBA layer is seen to be
439 remarkable consistent with winds from north-northwest between 4 and 7 km AMSL (**Figure 11d**), in
440 agreement with the backward trajectories in the northern part of the F06 flight track (**Figure 10a**). In
441 conclusion, the dropsonde-derived RH profile over Etosha between 5.5 and 7 km AMSL suggests large
442 scale ascending motion above the BBA layer over the continental plateau, as opposed to the nearby
443 ocean where the RH profile suggests strong subsidence associated with the South Atlantic high.
444 Enhanced ABC above 6 km AMSL is not related to differential transport of BBA layers of different origin,
445 but rather to the lifting of the top of the BBA layer (with non-negligible RH values contributing increase
446 lidar backscatter signal by hygroscopic growth of aerosols). The presence of black carbon tracers above
447 6 km AMSL is also seen in the Meso-NH simulation (**Figure 9b**). Backward trajectories computed
448 between 6 and 7 km AMSL in that area (between kilometres 400 and 1000 in **Figure 9a**) are nearly all
449 associated with air masses from the northeast, i.e. the fires prone regions of Angola and Zambia. These
450 backward trajectories are seen to upglide to almost 8.5 km AMSL in the 24 h preceding their arrival
451 over the Etosha pan region (not shown). This provides further confirmation of ascending motion above
452 the BBA layer over the Etosha pan region, consistent with air moving in the easterly low wave.

453 4.4 Analysis of BBA transport on 6 September

454 **Figure 12** shows the backward trajectories ending at 1200 UTC between 1 and 7 km AMSL, along the
455 F09 flight track on 6 September. Backward trajectories between 1 and 5 km AMSL (**Figure 12a, c, d**)
456 are very similar to those seen on 5 September, with air masses having travelled over Angola, Zambia,
457 Zimbabwe and Mozambique before reaching northern Namibia. The black carbon tracer
458 concentrations increase along the path of the trajectories towards Namibia (**Figure S5d**). On both 5
459 and 6 September, the air masses originate from the north east (**Figure 12**), ending between 4 and 5
460 km AMSL. All trajectories show significant lofting in the previous 24 h prior to reaching the area of the
461 Falcon flight. Above, the backward trajectories ending along the flight track are essentially coming from
462 the southeast and are descending from 11 to 7 km upon reaching the area of interest (**Figure 12b**).
463 Only a few trajectories ending in the Etosha pan region originate from the northeast (as opposed to
464 the previous day when a significant number of such trajectories were seen). On this day, vertical
465 motion above the BBA layer is dominated by subsiding dry air masses travelling along the southern
466 fringes of the CoL during the previous 3 days (**Figure S5c**). On 6 September, these descending
467 trajectories extend much further over the ocean than on the previous day (compare **Figure 10b** and
468 **Figure 12b**). This is consistent with the fact that the CoL was well established over the area of the flight
469 two days prior to the flight (i.e. on 4 September, **Figure 3d**), more so than the CoL on 3 September
470 (**Figure 3c**) two days prior to the flight on 5 September. As a result of the dominance of the descending
471 air masses over northern Namibia, a sharp RH transition to very dry conditions is observed at the top
472 the BBA layer, above 6.5 km AMSL, along the southern part of the F09 flight track (**Figure 11e**).
473 Likewise, the top of the BBA layer over Etosha is significantly lower than on the previous day, even
474 though the structure of the RH profile in the upper part of the BBA layer suggest weaker ascending
475 motion (**Figure 11f**) than on 5 September. The RH and potential temperature profiles acquired over
476 the Etosha pan confirm the presence of a deeper convective boundary layer on 6 September (with a
477 top at 4 km AMSL) due to the fact that the flight took place later in the day than on 5 September (the
478 top of the convective boundary layer being observed at 2 km AMSL). The maxima of RH are observed
479 to be slightly higher on 6 September (~80%, **Figure 11f**) than on the previous day (~70%, **Figure 11c**).

480

481 5. The impact of the CoL and the TTT on the tropospheric composition over the sub-continent

482 In the previous section, we showed that the mid-tropospheric circulation associated with the presence
483 of the CoL potentially modulates the depth of the underlying widespread layer of the smoke layer over



484 northern Namibia. The modulation appears to be forced by the vertical motion associated with the
485 CoL, i.e. subsiding air parcels to the south and west of its centre, and ascending motion to the north
486 and east of it. In the following, we provide further evidence of this modulation over northern Namibia,
487 where the CoL was observed to be intense during two days (3 and 4 September) by looking at the
488 evolution of the vertical distribution of black carbon tracers and potential vorticity, among other
489 variables, using Meso-NH simulations and ERA5 reanalysis.

490 The horizontal extent of the CoL over Northern Namibia and more particularly above three sun-
491 photometer stations (namely Henties Bay, Windpoort and Bonanza) on 3 and 4 September 2017 was
492 highlighted using ERA5-derived potential vorticity (PV) in **Figure 3**. The time-height section of the PV
493 over Windpoort from 1 to 6 September (**Figure 13a**) evidences the presence of the CoL from mid-day
494 on 2 September until the end of 4 September, associated with negative PV (less than $4 \cdot 10^{-6} \text{ K m}^2 \text{ kg}^{-1} \text{ s}^{-1}$)
495 and cyclonic circulation, between 400 and 300 hPa. In the lower troposphere, the shallow nocturnal
496 boundary layer is also associated with negative PV and cyclonic circulation. The top of the nocturnal
497 boundary layer is found around 875 hPa. In comparison, the deeper daytime PBL is associated with
498 positive PV and anticyclonic circulation. The strongest ascending motions in the mid-troposphere (800-
499 400 hPa) is seen between 1200 UTC on 2 September and 1200 UTC on 3 September (**Figure 13b**). This
500 strong vertical motion is associated with the sloping negative PV structure related to the incoming CoL
501 (**Figure 13a**). Concomitantly, RH above 600 hPa increases dramatically up to 400 hPa at 1200 UTC on 3
502 September (**Figure 13c**), together with the cloud cover (**Figure 13d**). The cloud cover is found to
503 decrease after 3 September, unlike RH that remains high above 600 hPa in the following days. The
504 peak in cloud cover over Windpoort on 3 September is consistent with the space-borne observations
505 made with SEVIRI (**Figure S6b**) which shows the presence of an isolated patch of mid-level clouds south
506 of the Etosha pan region on 2 September at 1200 UTC and over the area of Etosha on 3 September at
507 1200 UTC (**Figure S6a,b**). Overall, the mid-level cloud cover above continental Namibia is low and the
508 isolated nature of the mid-level cloud patches on 2 and 3 September suggests that they are formed
509 locally rather than being advected from another area. On 4 September, the space-borne lidar CATS
510 overpassed northern Namibia, just to the north of the Etosha pan during the daytime and across the
511 CoL (**Figure 6a**). The CATS observations evidence that the PBL is the deepest seen over the continental
512 plateau along the transect (**Figure S6d**) and that mid-level clouds are forming on top of the PBL to the
513 north of the centre of the CoL. This is also a strong evidence that the CoL generates strong local
514 ascending motion in the lower troposphere leading to the formation of an isolated cloud patch, also
515 visible on the SEVIRI images (**Figure S6c**).

516 The Meso-NH-derived time-height evolution of smoke tracer concentrations, vorticity and cloud liquid
517 water over Windpoort between 1 and 6 September 2017 is shown in **Figure 14a**. Even though the
518 largest black carbon tracer concentrations are seen after 1200 UTC on 5 September (i.e. the time when
519 the airborne observations discussed above were acquired), the simulation shows that the deepest BBA
520 layer over Windpoort occurred late on 3 September (1200-2100 UTC) as well as late on 4 September
521 (1800-2100 UTC) in connection with the presence of CoL-related potential vorticity in the upper-
522 troposphere reaching towards the surface to altitudes between 6 and 7 km AMSL. On this occasion,
523 the top of the BBA layer reaches at least 8 km AMSL, while later on, i.e. on 5 and 6 September, the top
524 of the BBA layer is between 6 and 6.5 km AMSL as with the airborne lidar measurements in the area
525 of Windpoort. The liquid water content at the top of the BBA layer increases from 1 to 3 September,
526 together with the height of the condensation level (**Figure 14a**), both variables reaching their
527 maximum values late on 3 September, i.e. shortly after the descent of mid-tropospheric vorticity on
528 that day. On 4 and 5 September, the level of condensation is much lower (between 4 and 6 km AMSL)
529 and within the BBA layer, in accordance with the lidar observations. Further south, in Upington (**Figure**
530 **14b**), the presence of mid-tropospheric potential vorticity at altitudes as low as 7 km AMSL around
531 mid-day on 5 September. Later that day, Meso-NH simulates the deepest BBA layer of the period, the
532 top of the layer reaching between 7 and 8 km AMSL. The simulation reproduces consistently the
533 sporadic nature of the event in Upington associated with the advection of the river of smoke observed
534 in Section 4, with large black carbon tracer concentrations occurring late on 5 September, over a large



535 depth in the lower troposphere. It is worth noting that liquid water is seen to extend from 4 to 7 km
536 AMSL, thereby suggesting thick clouds embedded in the river of smoke, in accordance with
537 observations from MODIS (horizontal distribution, **Figure 6**) and from CATS (vertical distribution,
538 **Figure 7**) as well as from SEVIRI regarding clouds (**Figure S6**).

539 The characteristics of the river of smoke (timing, vertical extent of the BBA layer) seen in Upington
540 based on Meso-NH simulations cannot be seen further north (e.g. in Windpoort) as northern Namibia
541 was under the influence of a well formed, stationary, isolated CoL on 3 and 4 September (**Figure 3c**,
542 **d**), unlike South Africa over which the fast evolving CoL travelled south-eastward between 5 and 6
543 September while merging back with the main westerly flow (**Figure 3e, f**). Hence, the picture emerges
544 that the characteristics of the river of smoke are very much tied to the later (fast evolving) stage of the
545 evolution of the CoL than the earlier (stationary) stage. The model results discussed in this section
546 highlight the mechanisms by which the CoL observed over southern Africa at the beginning of
547 September 2017 influences the vertical structure of the BBA layer, essentially through the CoL-related
548 ascending/descending motion above the BBA layer. The deepest BBA layers over northern Namibia
549 could not be observed with the airborne platform operated during AEROCLO-sA. Nevertheless, the
550 Meso-NH simulation for the period 5-6 September being very consistent with the observations
551 gathered during the campaign, we are confident that the Meso-NH-derived structure of the BBA layer
552 over northern Namibia during the stationary phase of the CoL is realistic.

553

554 **6. Conclusions**

555 The formation of a river of smoke crossing southern Africa has been investigated during the Aerosols,
556 Radiation and Clouds in southern Africa (AEROCLO-sA) campaign for 2 to 6 September 2017 in
557 connection with a mid-level TTT and a CoL, using a complementary set of global and mesoscale
558 numerical simulations as well as ground-based, airborne and space-borne observations.

559 Numerical simulations performed with the high resolution Meso-NH model together with space-borne
560 lidar observation made with CATS provide evidence that the top of the BBA layer over northern
561 Namibia (where the CoL remained stationary for 2 days) may reach altitudes higher than of 8 km AMSL.
562 This is much higher than the height of the top of the BBA layer over the regions where the smoke
563 originates from (Angola, Zambia, Zimbabwe, Mozambique), i.e. ~5 to 6 km AMSL. The impact of the
564 CoL-driven TTT on the vertical distribution of BBA was also felt further south, over South Africa, in the
565 form of a river of smoke as the CoL was rapidly travelling southwestward before merging with the
566 westerlies. The TTT created favourable conditions for efficiently transporting BBA-prone tropical air
567 masses towards the southwestern Indian Ocean. The temporal evolution of the river of smoke was
568 found to be connected to the fast evolving stage of the CoL. Besides favouring the increase of the BBA
569 layer top, the ascending motion associated with the CoL also promoted the occurrence of mid-level
570 clouds over northern Namibia in the early (stationary) phase of the CoL evolution (2-4 September,
571 **Figure 15a**) while cloud-free conditions were observed everywhere else over the continent. In the fast
572 evolving stage of the CoL (5 and 6 September, **Figure 15b and 15c**, respectively), a band of mid-level
573 clouds was embedded in the river of smoke that were related to the circulation in the lee of the CoL.

574 Even though the CoL observed on 3-6 September 2017 did not impact the circulation at the surface
575 directly, the Meso-NH simulation provides unambiguous evidence that the river of smoke event that
576 swept through western South Africa (i.e. away from the region of fires) not only had a mid-tropospheric
577 signature, but also that air quality associated with the transported BBA was reaching the surface, as
578 illustrated in Upington. Such behaviour was also observed during SAFARI 2000 by Magi et al. (2003)
579 and Schmid et al. (2003). These authors have also shown that the height of the top of the BBA layer
580 decreased significantly from northwest to southeast, i.e. between fire-prone regions in the Tropics and
581 the exit region of the river of smoke. The altitude of the top of the BBA layer observed during AEROCLO-
582 sA is consistent with that measured over Zambia during SAFARI2000 (Schmid et al., 2003).



583 To the author's knowledge, this is the first time the link between the CoL dynamics and the formation
584 of a river of smoke is established. The CoL was an essential ingredient of the TTT that developed across
585 southern Africa. TTTs are known to compose the dominant rainfall-producing weather system over
586 southern Africa during the austral summer. Here, we demonstrate that TTTs also play a role in the
587 transport of BBA during the winter.

588 Future research will aim at consolidating our understanding of the impact of the main dynamical
589 features highlight in this study (CoL, TTT, Angola low) on the formation and the evolution of rivers of
590 smoke over the southern Africa sub-continent. Among overarching open questions to be investigated
591 using ERA5/CAMS reanalysis and satellite aerosols products, we shall assess: (1) what is the frequency
592 "rivers of smoke" during the austral winter, (2) how important is this mechanism for the transport of
593 CO and aerosols out of southern Africa compared to the other transport patterns identified by
594 Garstang et al. (1996), (3) whether CoLs and/or TTTs are systematically associated with rivers of smoke
595 and (4) what is the importance/role of the Angola low in promoting the accumulation of BBA in the
596 tropical band prior to their injection in smoke rivers.

597



598 **Data availability.** The aircraft data acquired specifically in the framework of the project and used here
599 can be accessed via the AEROCLO-sA database at <https://baobab.sedoo.fr/AEROCLO/> and now have
600 DOIs. The LNG lidar data DOI is <https://doi.org/10.6096/AEROCLO.1774>. The dropsondes data DOI is
601 <https://doi.org/10.6096/AEROCLO.1777>. The Meso-NH-derived fields and back trajectories data can
602 be obtained upon request to the corresponding author of the paper. AERONET products can be
603 accessed at <https://aeronet.gsfc.nasa.gov/>. IASI data can be obtained via the AERIS data center
604 (<https://iasi.aeris-data.fr>). SEVIRI imagery can be accessed via <http://aeroclo.sedoo.fr/>. MODIS data is
605 accessible via <https://giovanni.gsfc.nasa.gov/giovanni/>. SEVIRI images are available via EUMETSAT
606 (European Organisation for the Exploitation of Meteorological Satellites).

607 **Author contributions.** CF processed and analysed the airborne lidar data and the dropsonde data as
608 well as the Meso-NH simulations, ERA5 and CAMS reanalysis, and wrote the paper. MG assembled the
609 material from ECMWF (ERA5 and CAMS), prepared the related figures, and contributed to the
610 interpretation of the atmospheric dynamic and composition data. PC gathered the CATS lidar data and
611 the MODIS data, and produced the related figures. JPC performed the Meso-NH simulation and
612 produced the related figures. SJP contributed to the analysis of the synoptic conditions. JC collected
613 CO data from IASI and produced the corresponding figure. PF coordinated the AEROCLO-sA project. All
614 have contributed to the writing of the paper.

615 **Competing interests.** Paola Formenti is guest editor for the ACP Special Issue “New observations and
616 related modelling studies of the aerosol–cloud–climate system in the Southeast Atlantic and southern
617 Africa regions”. The remaining authors declare that they have no conflicts of interests.

618 **Special issue statement.** This article is part of the special issue “New observations and related
619 modelling studies of the aerosol–cloud–climate system in the Southeast Atlantic and southern Africa
620 regions (ACP/AMT inter-journal SI)”. It is not associated with a conference.

621 **Acknowledgments.** The authors thank the AERIS data centre for their support during the campaign
622 and managing the AEROCLO-sA database. Airborne data was obtained using the aircraft managed by
623 SAFIRE, the French facility for airborne research, an infrastructure of the French National Centre for
624 Scientific Research (CNRS), Météo-France and the French space agency CNES. The authors thank F.
625 Blouzon and A. Abchiche (DT-INSU) as well as P. Genau and M. van Haecke (LATMOS) for their support
626 in operating and processing the LNG data. The invaluable diplomatic assistance of the French Embassy
627 in Namibia, the administrative support of the Service Partnership and Valorisation of the Regional
628 Delegation of the Paris-Villejuif Region of the CNRS, and the cooperation of the Namibian National
629 Commission on Research, Science and Technology (NCRST) are sincerely acknowledged. The authors
630 acknowledge the MODIS science, processing and data support teams for producing and providing
631 MODIS data (at <https://modis.gsfc.nasa.gov/data/dataprod/>). The authors thank the AERONET
632 network for sun-photometer products. IASI is a joint mission of EUMETSAT and the Centre National
633 d’Etudes Spatiales (CNES, France). The authors acknowledge the AERIS data centre for providing access
634 to the CO IASI data in this study as well as the Université Libre de Bruxelles and LATMOS for the
635 development of the retrieval algorithms.

636 **Financial support.** This work was supported by the French National Research Agency under grant
637 agreement n° ANR-15-CE01-0014-01, the French national program LEFE/INSU, the Programme
638 national de Télédétection Spatiale (PNTS, <http://programmes.insu.cnrs.fr/pnts/>), grant n° PNTS-2016-
639 14, the French National Agency for Space Studies (CNES), and the South African National Research
640 Foundation (NRF) under grant UID 105958. The research leading to these results has received funding
641 from the European Union’s 7th Framework Programme (FP7/2014-2018) under EUFAR2 contract
642 n°312609. Computer resources for running Meso-NH were allocated by GENCI through project 90569.

643



644 **References**

- 645 Annegarn, H. J., L. Otter, R. J. Swap, and R. J. Scholes: Southern Africa's ecosystem in a test-tube: A
646 perspective on the Southern African Regional Science Initiative (SAFARI 2000), *S. Afr. J. Sci.*, 98, 111–
647 113, 2002.
- 648 Bruneau, J., J. Pelon, F. Blouzon, J. Spatazza, P. Genau, G. Buchholtz, N. Amarouche, A. Abchiche and
649 O. Aouji: 355-nm high spectral resolution airborne lidar LNG: system description and first results,
650 *Applied optics*, 54, 8776–8785, <https://doi.org/10.1364/AO.54.008776>, 2015.
- 651 Bergstrom, R. W., Pilewskie, P., Russell, P. B., Redemann, J., Bond, T. C., Quinn, P. K., and Sierau, B.:
652 Spectral absorption properties of atmospheric aerosols, *Atmos. Chem. Phys.*, 7, 5937–5943,
653 <https://doi.org/10.5194/acp-7-5937-2007>, 2007.
- 654 Clerbaux, C., Boynard, A., Clarisse, L., George, M., Hadji-Lazaro, J., Herbin, H., Hurtmans, D., Pommier,
655 M., Razavi, A., Turquety, S., Wespes, C., and Coheur, P.-F.: Monitoring of atmospheric composition
656 using the thermal infrared IASI/MetOp sounder, *Atmos. Chem. Phys.*, 9, 6041–6054,
657 <https://doi.org/10.5194/acp-9-6041-2009>, 2009.
- 658 Chaboureaud, J.-P. and P. Bechtold: A simple cloud parameterization from cloud resolving model data:
659 Theory and application, *J. Atmos. Sci.*, 59, 2362–2372, [https://doi.org/10.1175/1520-0469\(2002\)059%3C2362:ASCPDF%3E2.0.CO;2](https://doi.org/10.1175/1520-0469(2002)059%3C2362:ASCPDF%3E2.0.CO;2), 2002.
- 661 Chapman, S., and R.S. Lindzen: *Atmospheric Tides*, Gordon and Breach, New York, 200 Pp, doi:
662 10.1007/978-94-010-3399-2, 1970.
- 663 Chazette, P., C. Flamant, J. Totems, M. Gaetani, G. Smith, A. Baron, X. Landsheere, K. Desboeufs, J.-F.
664 Doussin, and P. Formenti: Evidence of the complexity of aerosol transport in the lower troposphere on
665 the Namibian coast during AEROCLO-sA, *Atmos. Chem. Phys.*, 19, 14979–15005,
666 <https://doi.org/10.5194/acp-19-14979-2019>, 2019.
- 667 Cuxart, J., Bougeault, Ph. and Redelsperger, J.L.: A turbulence scheme allowing for mesoscale and
668 large-eddy simulations. *Q. J. R. Meteorol. Soc.*, 126, 1–30, <https://doi.org/10.1002/qj.49712656202>,
669 2000.
- 670 De Wachter, E., Barret, B., Le Flochmoën, E., Pavelin, E., Matri-cardi, M., Clerbaux, C., Hadji-Lazaro, J.,
671 George, M., Hurtmans, D., Coheur, P.-F., Nedelec, P., and Cammas, J. P.: Retrieval of MetOp-A/IASI CO
672 profiles and validation with MOZAIIC data, *Atmos. Meas. Tech.*, 5, 2843–2857,
673 <https://doi.org/10.5194/amt-5-2843-2012>, 2012.
- 674 Dufлот, V., B. Dils, J. L. Baray, M. De Mazière, J. L. Attié, G. Vanhaelewyn, C. Senten, C. Vigouroux, G.
675 Clain, and R. Delmas: Analysis of the origin of the distribution of CO in the subtropical southern Indian
676 Ocean in 2007, *J. Geophys. Res.*, 115, D22106, doi:10.1029/2010JD013994, 2010.
- 677 Favre, A., Hewitson, B., Tadross, M., Lennard, C., and Cerezo-Mota, R.: Relationships between cut-off
678 lows and the semiannual and southern oscillations, *Clim. Dyn.*, 38: 1473–1482,
679 <https://doi.org/10.1007/s00382-011-1030-4>, 2012.
- 680 Formenti, P., B. D'Anna, C. Flamant, M. Mallet, S. J. Piketh, K. Schepanski, F. Waquet, F. Auriol, G.
681 Brogniez, F. Burnet, J.-P. Chaboureaud, A. Chauvigné, P. Chazette, C. Denjean, K. Desboeufs, J.-F.
682 Doussin, N. Elguidi, S. Feuerstein, M. Gaetani, C. Giorio, D. Klopper, M. D. Mallet, A. Monod, P. Nabat,
683 F. Solmon, A. Namwoonde, C. Chikwililwa, R. Mushi, E. J. Welton, and B. Holben, 2019: The Aerosols,
684 Radiation and Clouds in southern Africa (AEROCLO-sA) field campaign in Namibia: overview, illustrative
685 observations and way forward, *Bull. Am. Meteorol. Soc.*, 100, 1277–1298,
686 <https://doi.org/10.1175/BAMS-D-17-0278.1>, 2019
- 687 Fouquart, Y., and B. Bonnel: Computations of solar heating of the earth's atmosphere: A new
688 parametrization. *Beitr. Phys. Atmosph.*, 53, 35–62, 1980.



- 689 Gaetani, M., Pohl, B., Alvarez Castro, M. C., Flamant, C., and Formenti, P.: A weather regime
690 characterisation of winter biomass aerosol transport from southern Africa, *Atmos. Chem. Phys.*
691 *Discuss.*, in press, <https://doi.org/10.5194/acp-2021-337>, 2021.
- 692 Garstang, M., P. D. Tyson, R. Swap, M. Edwards, P. Kallberg, and J. A. Lindesay: Horizontal and vertical
693 transport of air over southern Africa, *J. Geophys. Res.*, 101, 23,721–23,736,
694 <https://doi.org/10.1029/95JD00844>, 1996.
- 695 George, M., Clerbaux, C., Hurtmans, D., Turquety, S., Coheur, P.-F., Pommier, M., Hadji-Lazaro, J.,
696 Edwards, D. P., Worden, H., Luo, M., Rinsland, C., and McMillan, W.: Carbon monoxide dis-
697 tributions from the IASI/METOP mission: evaluation with other space-borne remote sensors, *Atmos. Chem.*
698 *Phys.*, 9, 8317–8330, <https://doi.org/10.5194/acp-9-8317-2009>, 2009.
- 699 Gheusi, F., and J. Stein: Lagrangian description of airflows using Eulerian passive tracers, *Quart. J. Roy.*
700 *Meteor. Soc.*, 128, 337–360, <https://doi.org/10.1256/00359000260498914>, 2002.
- 701 Grini, A., Tulet, P., and Gomes, L.: Dusty weather forecasts using the MesoNH mesoscale atmospheric
702 model, *J. Geophys. Res.*, 111, D19205, doi:10.1029/2005JD007007, 2006.
- 703 Haywood, J. M., Abel, S. J., Barrett, P. A., Bellouin, N., Blyth, A., Bower, K. N., Brooks, M., Carslaw, K.,
704 Che, H., Coe, H., Cotterell, M. I., Crawford, I., Cui, Z., Davies, N., Dingley, B., Field, P., Formenti, P.,
705 Gordon, H., de Graaf, M., Herbert, R., Johnson, B., Jones, A. C., Langridge, J. M., Malavelle, F., Partridge,
706 D. G., Peers, F., Redemann, J., Stier, P., Szpek, K., Taylor, J. W., Watson-Parris, D., Wood, R., Wu, H.,
707 and Zuidema, P.: The CLOUD–Aerosol–Radiation Interaction and Forcing: Year 2017 (CLARIFY-2017)
708 measurement campaign, *Atmos. Chem. Phys.*, 21, 1049–1084, [https://doi.org/10.5194/acp-21-1049-](https://doi.org/10.5194/acp-21-1049-2021)
709 [2021](https://doi.org/10.5194/acp-21-1049-2021), 2021.
- 710 Hersbach, H., Bell, B., Berrisford, P., Biavati, G., Horányi, A., Muñoz Sabater, J., Nicolas, J., Peubey, C.,
711 Radu, R., Rozum, I., Schepers, D., Simmons, A., Soci, C., Dee, D., and Thépaut, J.-N.: ERA5 hourly data
712 on single levels from 1979 to present, Copernicus Climate Change Service (C3S) Climate Data Store
713 (CDS), <https://doi.org/10.24381/cds.adbb2d47> (last access: 8 Nov 2021), 2018.
- 714 Howard, E., Washington, R., & Hodges, K. I.: Tropical lows in southern Africa: Tracks, rainfall
715 contributions, and the role of ENSO. *Journal of Geophysical Research: Atmospheres*, 124,
716 <https://doi.org/10.1029/2019JD030803>, 2019
- 717 Hurtmans, D., Coheur, P. F., Wespes, C., Clarisse, L., Scharf, O., Clerbaux, C., Hadji-Lazaro, J., George,
718 M., and Turquety, S.: FORLI radiative transfer and retrieval code for IASI, *J. Quant. Spectrosc. Ra.*, 113,
719 1391–1408, <https://dx.doi.org/10.1016/j.jqsrt.2012.02.036>, 2012.
- 720 Inness, A., Ades, M., Agustí-Panareda, A., Barré, J., Benedictow, A., Blechschmidt, A., Dominguez, J.,
721 Engelen, R., Eskes, H., Flemming, J., Huijnen, V., Jones, L., Kipling, Z., Massart, S., Parrington, M., Peuch,
722 V.-H., Razinger, M., Remy, S., Schulz, M., and Suttie, M.: CAMS global reanalysis (EAC4), Copernicus
723 Atmosphere Monitoring Service (CAMS) Atmosphere Data Store (ADS) [data set],
724 <https://ads.atmosphere.copernicus.eu/cdsapp#!/dataset/cams-global-reanalysis-eac4?tab=overview>
725 (last access: 8 Nov 2020), 2019.
- 726 Jury, M. R., and T. Freiman: The climate of tropical southern Africa during the SAFARI 2000 campaign,
727 *South African Journal of Science* 98, 527–533, 2002.
- 728 King, M. D., Kaufman, Y. J., Menzel, W. P., and Tanré, D.: Remote sensing of cloud, aerosol, and water-
729 vapor properties from the Moderate Resolution Imaging Spectrometer (MODIS), *IEEE T. Geosci.*
730 *Remote Sens.*, 30, 2–27, <https://doi.org/10.1109/36.124212>, 1992.
- 731 Lac, C., Chaboureaud, J.-P., Masson, V., Pinty, J.-P., Tulet, P., Escobar, J., Leriche, M., Barthe, C.,
732 Aouizerats, B., Augros, C., Aumond, P., Auguste, F., Bechtold, P., Berthet, S., Bielli, S., Bosseur, F.,
733 Caumont, O., Cohard, J.-M., Colin, J., Couvreur, F., Cuxart, J., Delautier, G., Dauhut, T., Ducrocq, V.,
734 Filippi, J.-B., Gazen, D., Geoffroy, O., Gheusi, F., Honnert, R., Lafore, J.-P., Lebeaupin Brossier, C., Libois,



- 735 Q., Lunet, T., Mari, C., Maric, T., Mascart, P., Mogé, M., Molinié, G., Nuissier, O., Pantillon, F., Peyrillé,
736 P., Pergaud, J., Perraud, E., Pianezze, J., Redelsperger, J.-L., Ricard, D., Richard, E., Riette, S., Rodier, Q.,
737 Schoetter, R., Seyfried, L., Stein, J., Suhre, K., Taufour, M., Thouron, O., Turner, S., Verrelle, A., Vié, B.,
738 Visentin, F., Vionnet, V., and Wautelet, P.: Overview of the Meso-NH model version 5.4 and its
739 applications, *Geosci. Model Dev.*, 11, 1929-1969, <https://doi.org/10.5194/gmd-11-1929-2018>, 2018.
- 740 Luo, C., N. Mahowald, T. Bond, P. Y. Chuang, P. Artaxo, R. Siefert, Y. Chen, and J. Schauer: Combustion
741 iron distribution and deposition, *Global Biogeochem. Cycles*, 22, GB1012, doi:10.1029/2007GB002964,
742 2008.
- 743 Lyons, S. W.: Origins of convective variability over equatorial southern Africa during austral summer.
744 *J. Climate*, 4, 23–39, [https://doi.org/10.1175/1520-0442\(1991\)004<0023:OOCVOE>2.0.CO;2](https://doi.org/10.1175/1520-0442(1991)004<0023:OOCVOE>2.0.CO;2), 1991.
- 745 Macron C, B. Pohl, Y. Richard, and M. Bessafi: How do Tropical Temperate Troughs Form and Develop
746 over Southern Africa? *J. Climate*, 27, 1633-1647, <https://doi.org/10.1175/JCLI-D-13-00175.1>, 2014.
- 747 Magi, B. I., P. V. Hobbs, B. Schmid, and J. Redemann: Vertical profiles of light scattering, light
748 absorption, and single scattering albedo during the dry, biomass burning season in southern Africa and
749 comparisons of in situ and remote sensing measurements of aerosol optical depths, *J. Geophys. Res.*,
750 108(D13), 8504, doi:10.1029/2002JD002361, 2003.
- 751 Mallet, M., Nabat, P., Zuidema, P., Redemann, J., Sayer, A. M., Stengel, M., Schmidt, S., Cochrane, S.,
752 Burton, S., Ferrare, R., Meyer, K., Saide, P., Jethva, H., Torres, O., Wood, R., Saint Martin, D., Roehrig,
753 R., Hsu, C., and Formenti, P.: Simulation of the transport, vertical distribution, optical properties and
754 radiative impact of smoke aerosols with the ALADIN regional climate model during the ORACLES-2016
755 and LASIC experiments, *Atmos. Chem. Phys.*, 19, 4963–4990, [https://doi.org/10.5194/acp-19-4963-](https://doi.org/10.5194/acp-19-4963-2019)
756 [2019](https://doi.org/10.5194/acp-19-4963-2019), 2019.
- 757 Masson, V., P. Le Moigne, E. Martin, S. Faroux, A. Alias, R. Alkama, S. Belamari, A. Barbu, A. Boone, F.
758 Bouysse, P. Brousseau, E. Brun, J.-C. Calvet, D. Carrer, B. Decharme, C. Delire, S. Donier, K. Essauoui,
759 A.-L. Gibelin, H. Giordani, F. Habets, M. Jidane, G. Kerdraon, E. Kourzeneva, M. Lafaysse, S. Lafont, C.
760 Lebeaupin Brossier, A. Lemonsu, J.-F. Mahfouf, P. Marguinaud, M. Mokhtari, S. Morin, G. Pigeon, R.
761 Salgado, Y. Seity, F. Taillefer, G. Tanguy, P. Tulet, B. Vincendon, V. Vionnet, and A. Voltaire: The
762 SURFEXv7.2 land and ocean surface platform for coupled or offline simulation of earth surface
763 variables and fluxes, *Geosci. Model Dev.*, 6, 929-960, <https://doi.org/doi:10.5194/gmd-6-929-2013>,
764 2013.
- 765 McMillan, W., M. L. McCourt, H. E. Revercomb, R. O. Knuteson, T. J. Christian, B. G. Doddridge, P. V.
766 Hobbs, J. V. Lukovich, P. C. Novelli, S. J. Piketh, L. Sparling, D. Stein, R. J. Swap, and R. J. Yokelson:
767 Tropospheric carbon monoxide measurements from the Scanning High-resolution Interferometer
768 Sounder on 7 September 2000 in southern Africa during SAFARI 2000, *J. Geophys. Res.*, 108(D13), 8492,
769 doi:10.1029/2002JD002335, 2003.
- 770 Mlawer, E.J., S.J. Taubman, P.D. Brown, M.J. Iacono, and S.A. Clough: Radiative transfer for
771 inhomogeneous atmospheres: RRTM, a validated correlated-k model for the longwave. *J. Geophys.*
772 *Res.*, 102D, 16663-16682, <https://doi.org/10.1029/97JD00237>, 1997.
- 773 Pak, B. C., L. Langenfelds, S. A. Young, R. J. Francey, C. P. Meyer, L. M. Kivlighon, L. N. Cooper, B. L.
774 Dunse, C. E. Allison, L. P. Steele, I. E. Galbally, and I. A. Weeks: Measurements of biomass burning
775 influences in the troposphere over southeast Australia during the SAFARI 2000 dry season campaign,
776 *J. Geophys. Res.*, 108(D13), 8480, doi:10.1029/2002JD002343, 2003.
- 777 Pergaud, J., V. Masson, S. Malardel, and F. Couvreux: A parameterization of dry thermals and shallow
778 cumuli for mesoscale numerical weather prediction, *Bound.-Layer. Meteor.*, 132, 83-106,
779 <https://doi.org/10.1007/s10546-009-9388-0>, 2009.



- 780 Pinty, J.-P. and P. Jabouille, 1998: A mixed-phase cloud parameterization for use in mesoscale non-
781 hydrostatic model: simulations of a squall line and of orographic precipitations. Proc. Conf. of Cloud
782 Physics, Everett, WA, USA, Amer. Meteor. Soc., 217 – 220, 1999.
- 783 Randriamiarisoa, H., Chazette, P., Couvert, P., Sanak, J., and Mégie, G.: Relative humidity impact on
784 aerosol parameters in a Paris suburban area: Atmos. Chem. Phys., 6, 1389-1407,
785 <https://doi.org/10.5194/acp-6-1389-2006>, 2006.
- 786 Ratna, S.B., S. Behera, J.V. Ratnam, K. Takahashi, and T. Yamagata: An index for tropical temperate
787 troughs over southern Africa. Clim Dyn 41, 421–441. <https://doi.org/10.1007/s00382-012-1540-8>,
788 2013.
- 789 Redemann, J., Wood, R., Zuidema, P., Doherty, S. J., Luna, B., LeBlanc, S. E., Diamond, M. S., Shinozuka,
790 Y., Chang, I. Y., Ueyama, R., Pfister, L., Ryoo, J.-M., Dobracki, A. N., da Silva, A. M., Longo, K. M.,
791 Kacenelenbogen, M. S., Flynn, C. J., Pistone, K., Knox, N. M., Piketh, S. J., Haywood, J. M., Formenti, P.,
792 Mallet, M., Stier, P., Ackerman, A. S., Bauer, S. E., Fridlind, A. M., Carmichael, G. R., Saide, P. E., Ferrada,
793 G. A., Howell, S. G., Freitag, S., Cairns, B., Holben, B. N., Knobelspiesse, K. D., Tanelli, S., L'Ecuyer, T. S.,
794 Dzambo, A. M., Sy, O. O., McFarquhar, G. M., Poellot, M. R., Gupta, S., O'Brien, J. R., Nenes, A., Kacarab,
795 M., Wong, J. P. S., Small-Griswold, J. D., Thornhill, K. L., Noone, D., Podolske, J. R., Schmidt, K. S.,
796 Pilewskie, P., Chen, H., Cochrane, S. P., Sedlacek, A. J., Lang, T. J., Stith, E., Segal-Rozenhaimer, M.,
797 Ferrare, R. A., Burton, S. P., Hostetler, C. A., Diner, D. J., Seidel, F. C., Platnick, S. E., Myers, J. S., Meyer,
798 K. G., Spangenberg, D. A., Maring, H., and Gao, L.: An overview of the ORACLES (ObseRvations of
799 Aerosols above CLouds and their intEractionS) project: aerosol–cloud–radiation interactions in the
800 southeast Atlantic basin, Atmos. Chem. Phys., 21, 1507–1563, [https://doi.org/10.5194/acp-21-1507-](https://doi.org/10.5194/acp-21-1507-2021)
801 [2021](https://doi.org/10.5194/acp-21-1507-2021), 2021.
- 802 Roberts, G., Wooster, M. J., and Lagoudakis, E.: Annual and diurnal African biomass burning temporal
803 dynamics, Biogeosciences, 6, 849–866, <https://doi.org/10.5194/bg-6-849-2009>, 2009.
- 804 Schmid, B., J. Redemann, P. B. Russell, P. V. Hobbs, D. L. Hlavka, M. J. McGill, B. N. Holben, E. J. Welton,
805 J. R. Campbell, O. Torres, R. A. Kahn, D. J. Diner, M. C. Helmlinger, D. A. Chu, C. Robles-Gonzalez and G.
806 de Leeuw: Coordinated airborne, spaceborne, and ground-based measurements of massive, thick
807 aerosol layers during the dry season in southern Africa, J. Geophys. Res., 108(D13), 8496,
808 doi:10.1029/2002JD002297, 2003.
- 809 Sinha, P., L. Jaeglé, P. Hobbs, and Q. Liang: Transport of biomass burning emissions from southern
810 Africa, J. Geophys. Res., 109, D20204, <https://doi.org/10.1029/2004JD005044>, 2004.
- 811 Stein, D. C., R. J. Swap, S. Greco, S. J. Piketh, S. A. Macko, B. G. Doddridge, T. Elias, and R. T. Brientjes:
812 Haze layer characterization and associated meteorological controls along the eastern coastal region of
813 southern Africa, J. Geophys. Res., 108(D13), 8506, doi:10.1029/2002JD003237, 2003.
- 814 Swap, R. J., Annegarn, H. J., Suttles, J. T., King, M. D., Platnick, S., Privette, J. L., and Scholes, R. J.: Africa
815 burning: A thematic analysis of the Southern African Regional Science Initiative (SAFARI 2000), J.
816 Geophys. Res.-Atmos., 108, 8465–8479, <https://doi.org/10.1029/2003JD003747>, 2003.
- 817 Todd M. C., R. Washington and P. I. Palmer: Water vapour transport associated with tropical-
818 temperate trough systems over southern Africa and the southwest Indian Ocean, Int. J. Climatol. 24,
819 555–568, <https://doi.org/10.1002/joc.1023>, 2004.
- 820 von Storch, H. and Zwiers, F. W.: Statistical Analysis in Climate Research, Cambridge University Press,
821 Cambridge, ISBN 978-0-5116-1233-6, <https://doi.org/10.1017/CBO9780511612336>, 1999.
- 822 van der Werf, G. R., Randerson, J. T., Giglio, L., van Leeuwen, T. T., Chen, Y., Rogers, B. M., Mu, M., van
823 Marle, M. J. E., Morton, D. C., Collatz, G. J., Yokelson, R. J., and Kasibhatla, P. S.: Global fire emissions
824 estimates during 1997–2016, Earth Syst. Sci. Data, 9, 697–720, [https://doi.org/10.5194/essd-9-697-](https://doi.org/10.5194/essd-9-697-2017)
825 [2017](https://doi.org/10.5194/essd-9-697-2017), 2017.



- 826 Yorks, J. E., McGill, M. J., Palm, S. P., Hlavka, D. L., Selmer, P. A., Nowottnick, E. P., Vaughan, M. A.,
827 Rodier, S. D., and Hart, W. D.: An overview of the CATS level 1 processing algorithms and data products,
828 *Geophys. Res. Lett.*, 43, 4632–4639, <https://doi.org/10.1002/2016GL068006>, 2016.
- 829 Zuidema, P., Chang, P., Medeiros, B., Kirtman, B. P., Mechoso, R., Schneider, E. K., Toniazzi, T., Richter,
830 I., Small, R. J., Bellomo, K., Brandt, P., de Szoeko, S., Farrar, J. T., Jung, E., Kato, S., Li, M., Patricola, C.,
831 Wang, Z., Wood, R., & Xu, Z: Challenges and Prospects for Reducing Coupled Climate Model SST Biases
832 in the Eastern Tropical Atlantic and Pacific Oceans: The U.S. CLIVAR Eastern Tropical Oceans Synthesis
833 Working Group, *Bulletin of the American Meteorological Society*, 97(12), 2305-2328,
834 <https://journals.ametsoc.org/view/journals/bams/97/12/bams-d-15-00274.1.xml>, 2016a.
- 835 Zuidema, P., Redemann, J., Haywood, J., Wood, R., Piketh, S., Hipondoka, M., & Formenti, P.: Smoke
836 and Clouds above the Southeast Atlantic: Upcoming Field Campaigns Probe Absorbing Aerosol's Impact
837 on Climate, *Bulletin of the American Meteorological Society*, 97(7), 1131-1135,
838 <https://journals.ametsoc.org/view/journals/bams/97/7/bams-d-15-00082.1.xml>, 2016b.
- 839
- 840



841 **Table 1.** Correlation coefficients computed between the first and second principal components of
842 MSLP, geopotential height at 300 and 700 hPa and the first principal component of the organic matter
843 AOT. P-values are indicated in brackets.

	Explained variance	Correlation
Z300	56%	0.50 ($p < 0.01$)
Z700	74%	0.78 ($p < 0.01$)
MSLP	43%	0.01 ($p = 0.60$)

844



845 **Figures**

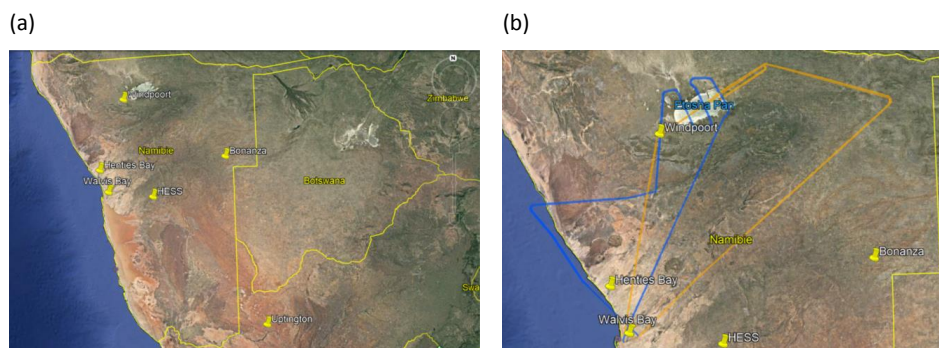


Figure 1: (a) Geographical map of Namibia and surrounding countries with the location of the main sites of interest: Walvis Bay (airport), Henties Bay (AEROCLO-SA main ground-based supersite) and AERONET stations in Windpoort, HESS, Bonanza (Namibia) and Upington (South Africa). (b) Zoom on northern Namibia where the Etosha pan is located (white area just northeast of Windpoort). The blue solid line represents the SAFIRE Falcon 20 flight track on 5 September in the morning (0736-1014 UTC) and the orange solid line represents the Falcon 20 flight track on 6 September afternoon (1055-1401 UTC). Map credit: © Google Earth 2021.

846

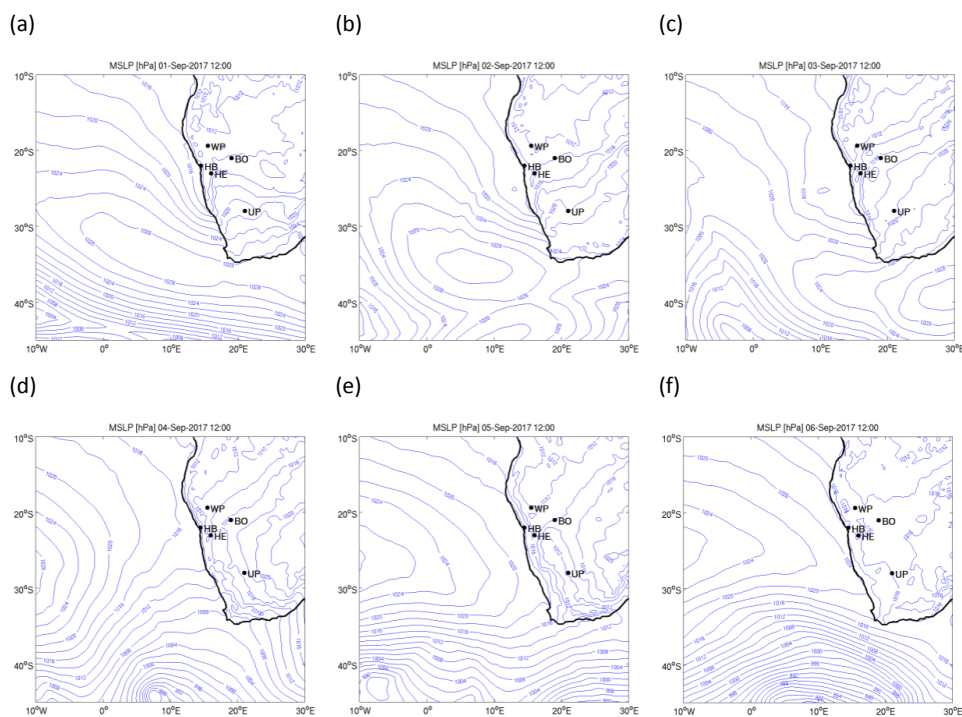


Figure 2: Mean sea level pressure (hPa) at 1200 UTC on (a) 1 September, (b) 2 September, (c) 3 September, (d) 4 September, (e) 5 September and (f) 6 September 2017, from ERA5 reanalysis. The names of the instrumented sites appear in black (from north to south): WP is Windpoort, BO is Bonanza, HB is Henties Bay, HE is HESS (Namibia) and UP is Uppington (South Africa).

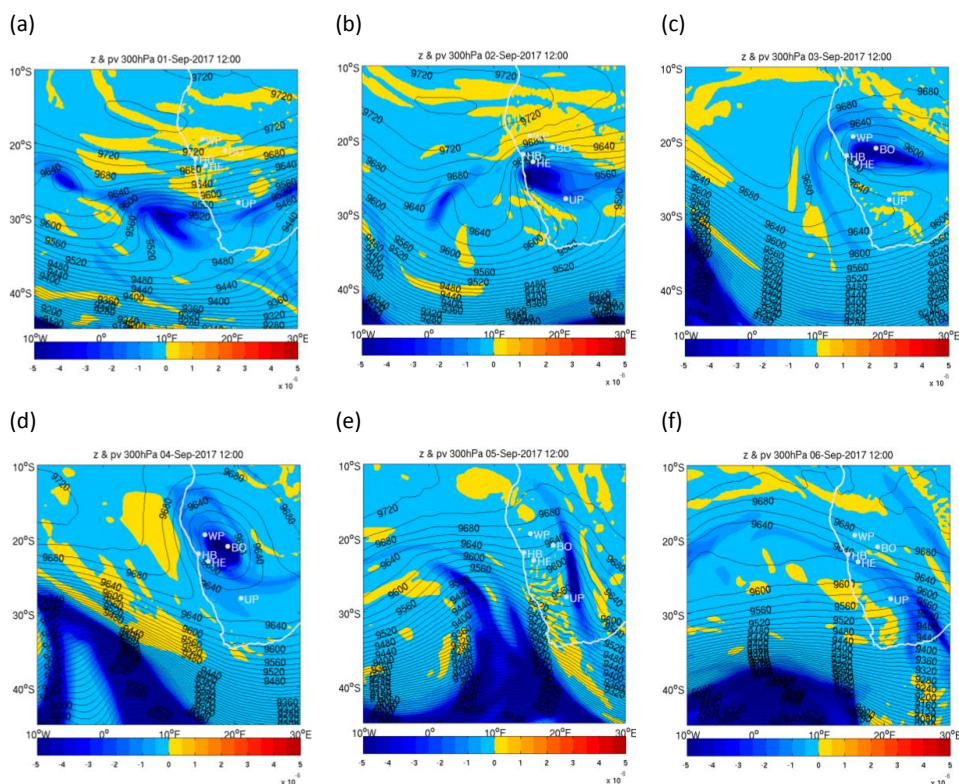


Figure 3: Geopotential (m, contours) and potential vorticity ($\text{K m}^2 \text{kg}^{-1} \text{s}^{-1}$, colour) at 300 hPa at 1200 UTC on (a) 01/09, (b) 02/09, (c) 03/09, (d) 04/09, (e) 05/09 and (f) 06/09 2017, from ERA 5 reanalysis. The names of the instrumented sites appear in white (from north to south): WP is Windpoort, BO is Bonanza, HB is Henties Bay, HE is HESS (Namibia) and UP is Upington (South Africa).

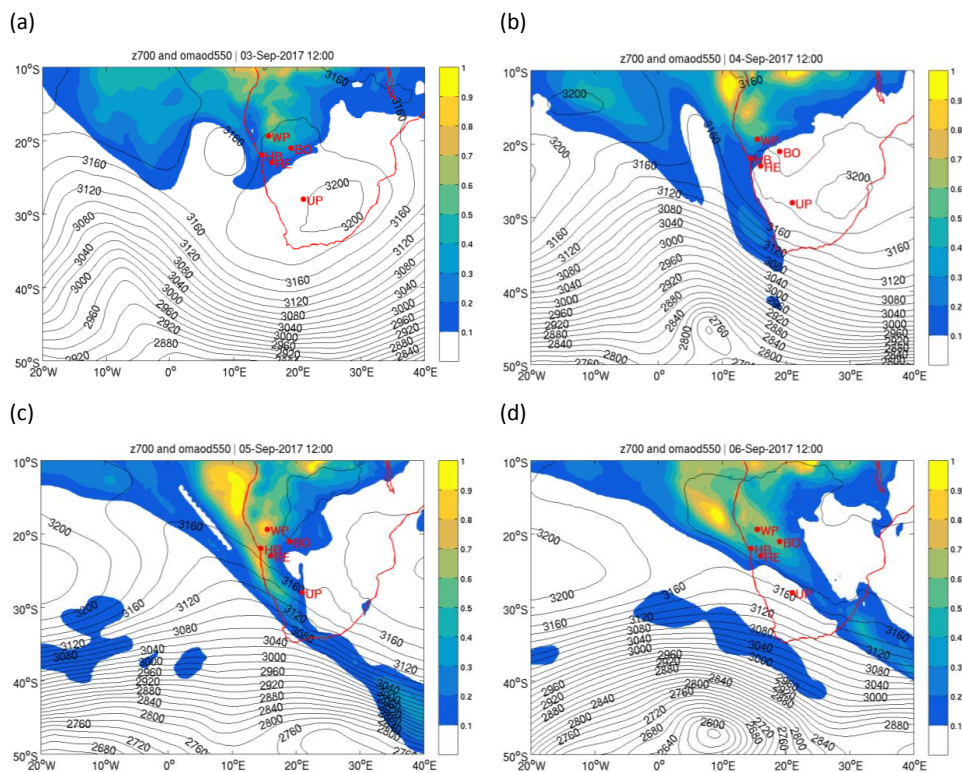


Figure 4: Geopotential at 700 hPa (contours) and organic matter AOT (colour) and 1200 UTC on (a) 03/09, (b) 04/09, (c) 05/09 and (d) 06/09 2017, from CAMS reanalysis. The names of the instrumented sites appear in red (from north to south): WP is Windpoort, BO is Bonanza, HB is Henties Bay, HE is HESS (Namibia) and UP is Upington (South Africa).

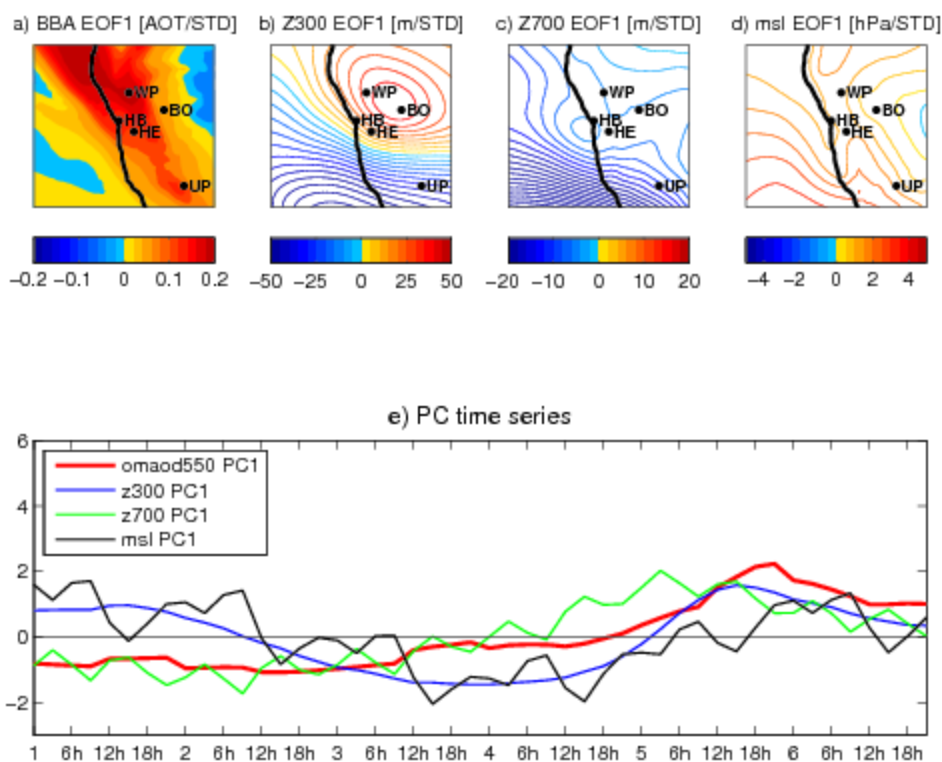


Figure 5: Principal component analysis (PCA) of CAMS BBA and atmospheric circulation above Namibia from 1 to 6 Sep 2017. In top panels, the anomaly patterns associated with the first mode of variability of (a) organic matter AOT at 550 nm, geopotential height at (b) 300 hPa and (c) 700 hPa, and (d) MSLP are obtained by regressing raw data onto the PCA time series displayed in panel (e). Anomaly patterns display anomalies per standard deviation (STD). The 12-h oscillation seen in the time series of the MSLP and the geopotential at 700 hPa is a tidal effect, typical of the Earth’s atmosphere (Chapman and Lindzen, 1970).

850

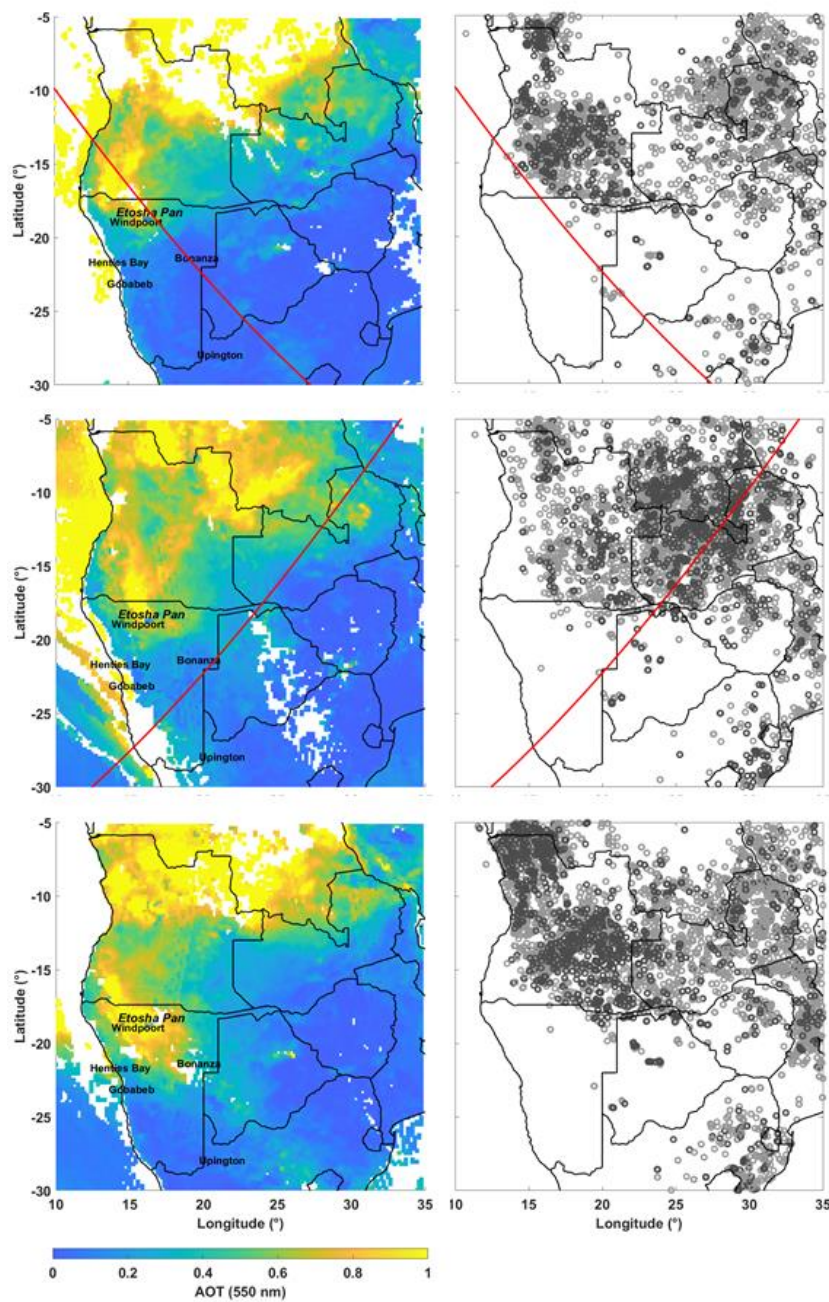


Figure 6 MODIS-derived AOT (left panels) on and Fire hot-spots location (right panels) derived from MODIS on 4 (a,b), 5 (c,d) and 6 (e,f) September 2017. The CATS tracks overpassing Namibia on 4 and 5 September are overlain on (a,b) and (c,d) as a solid red line. The confidence in the detection of the location of the fire hot spots is indicated by the colour of the circles (dark circles indicating high confidence and grey circles, nominal confidence, as provided by the MODIS team).

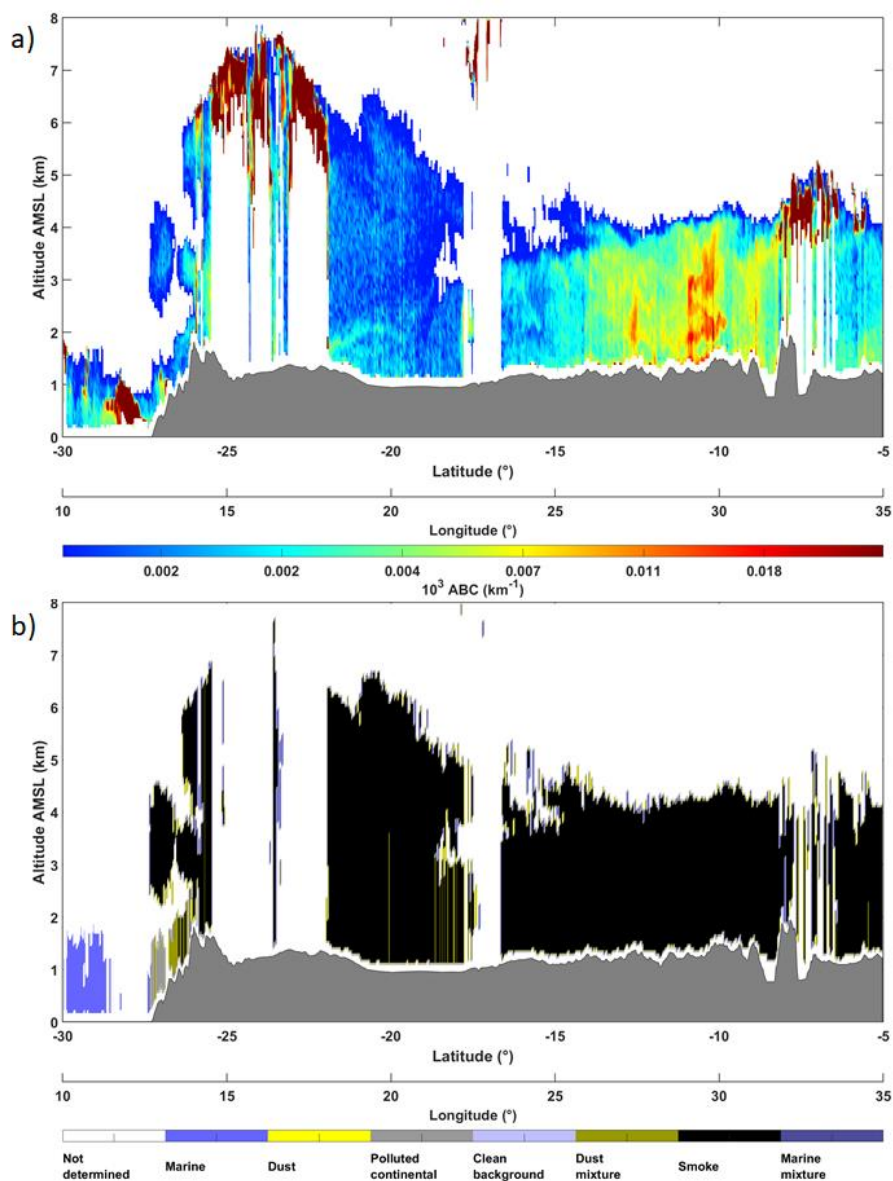


Figure 7: (a) Total attenuated backscatter coefficient from the space-borne lidar CATS between 22:05 and 22:21 UTC on 5 September 2017. (b) Same as (a), but for CATS-derived aerosol. The corresponding CATS track is shown in Figure 6b.

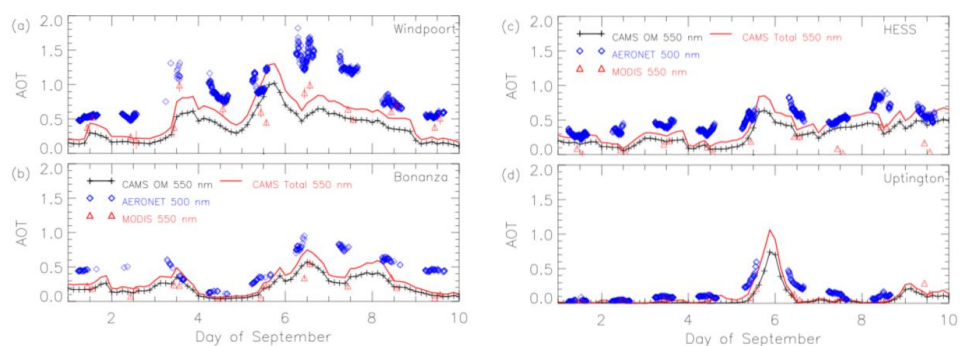


Figure 8: Time evolution of AERONET sun-photometer-derived total AOT (blue diamonds), MODIS AOT from Terra and Aqua (red triangles) and CAMS-derived total AOT (red solid line) and organic matter AOT (solid black line with black crosses) over (a) Windpoort, (b) Bonanza, (c) the HESS site and (d) Uptington from 1 to 10 September 2017.

852

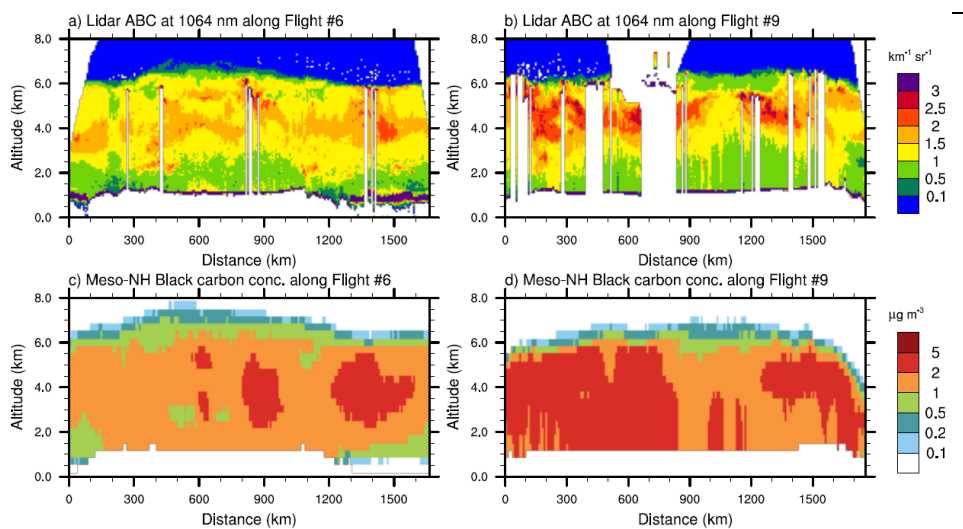


Figure 9: (a) Distance-height cross-section of attenuated backscatter coefficient derived at 1064 nm from LNG along the flight track of the Falcon 20 on 5 September from 0736 to 1014 UTC (see **Figure 1b**). (b) Black carbon tracer concentration as simulated with Meso-NH at 0900 UTC 5 September 2017 along the Falcon 20 flight track. (c) Same as (a) but on 6 September from 1055 to 1401 UTC. (d) Same as (b) but at 1200 UTC on 6 September.

853

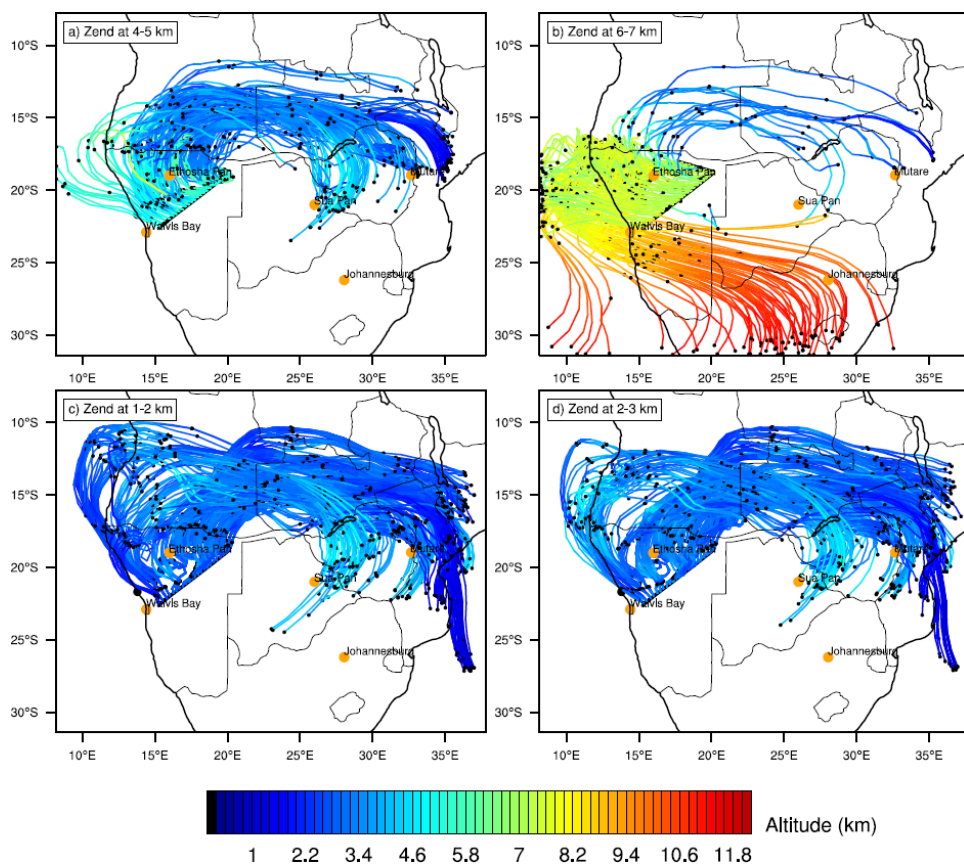


Figure 10: 102-h backward trajectories ending at 0900 UTC 5 September 2017 along the F06 flight track and at altitude between (a) 4 and 5 km AMSL, (b) 6 and 7 km AMSL, (c) 1 and 2 km AMSL and (d) 2 and 3 km AMSL. Dots on the backward trajectories are spaced at 24-h intervals. One backward trajectory out of 20 is plotted.

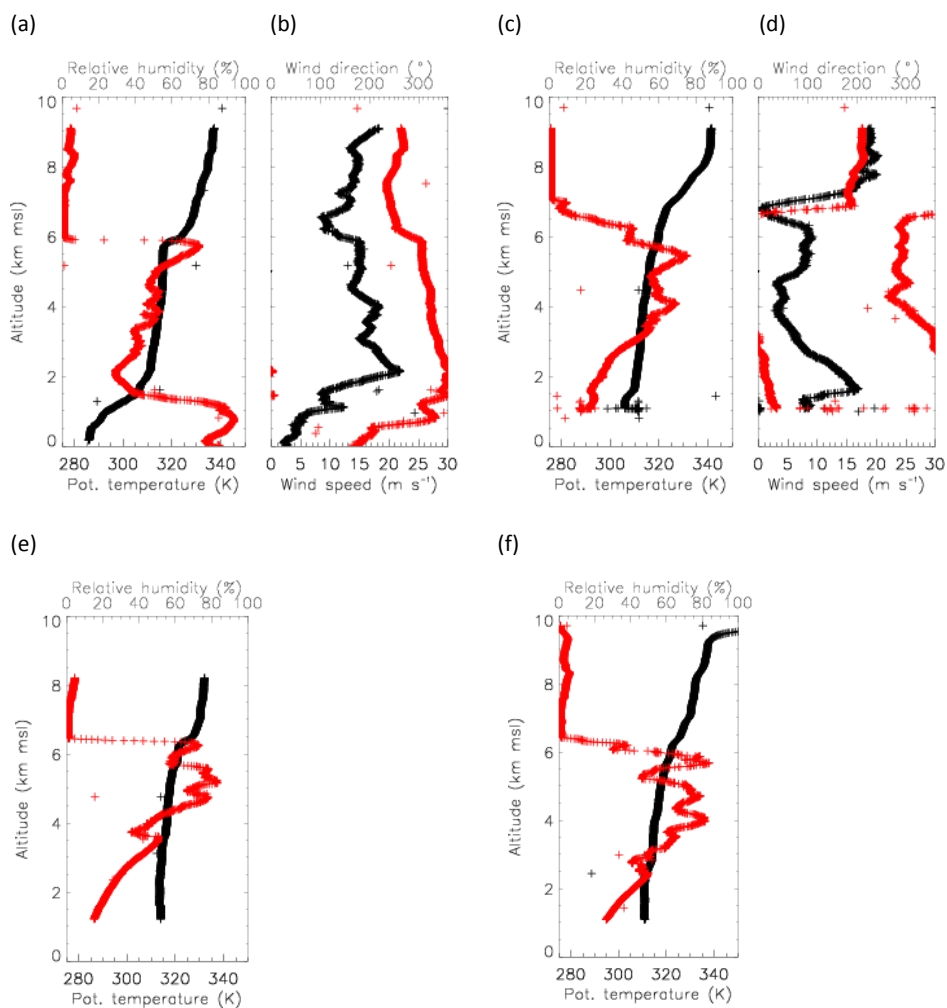


Figure 11: (a) Potential temperature (black) and relative humidity (red) profiles and (b) Wind speed (black) and wind direction (red) profiles derived from the dropsonde launched at 0951 UTC on 5 September. (c) and (d) same as (a) and (c), respectively, but for the dropsonde released at 0839 UTC. (e) Same as (a), but for the dropsonde released at 1337 UTC on 6 September. (f) Same as (e), but for the dropsonde released at 1146 UTC.

855

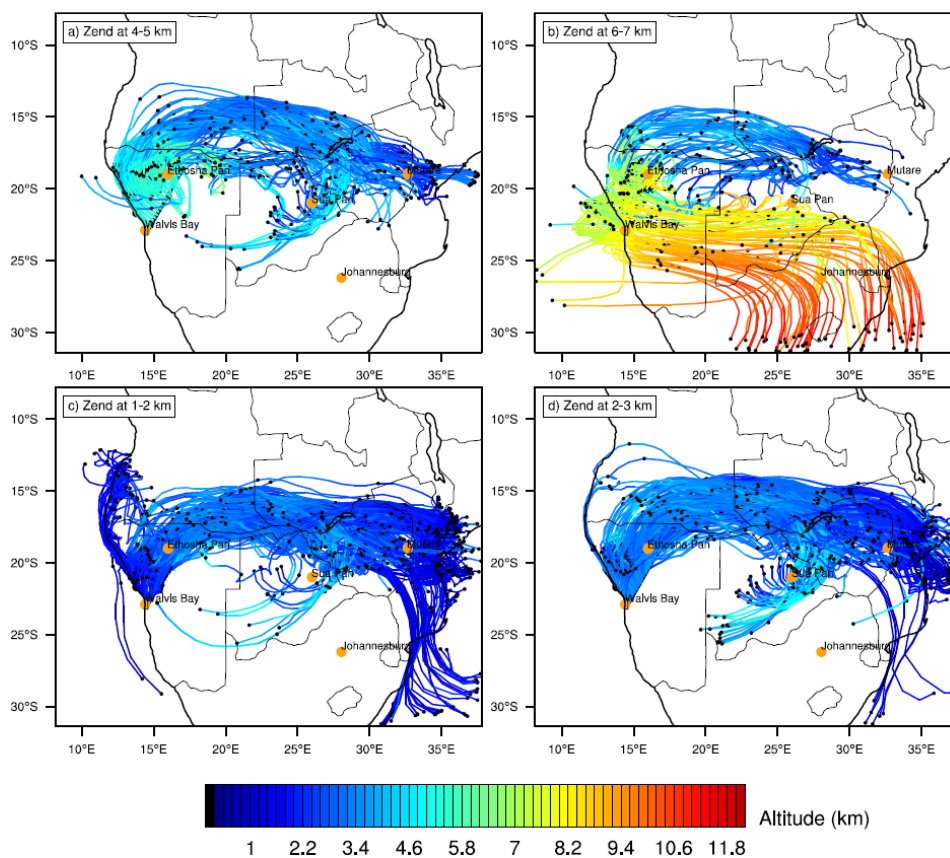
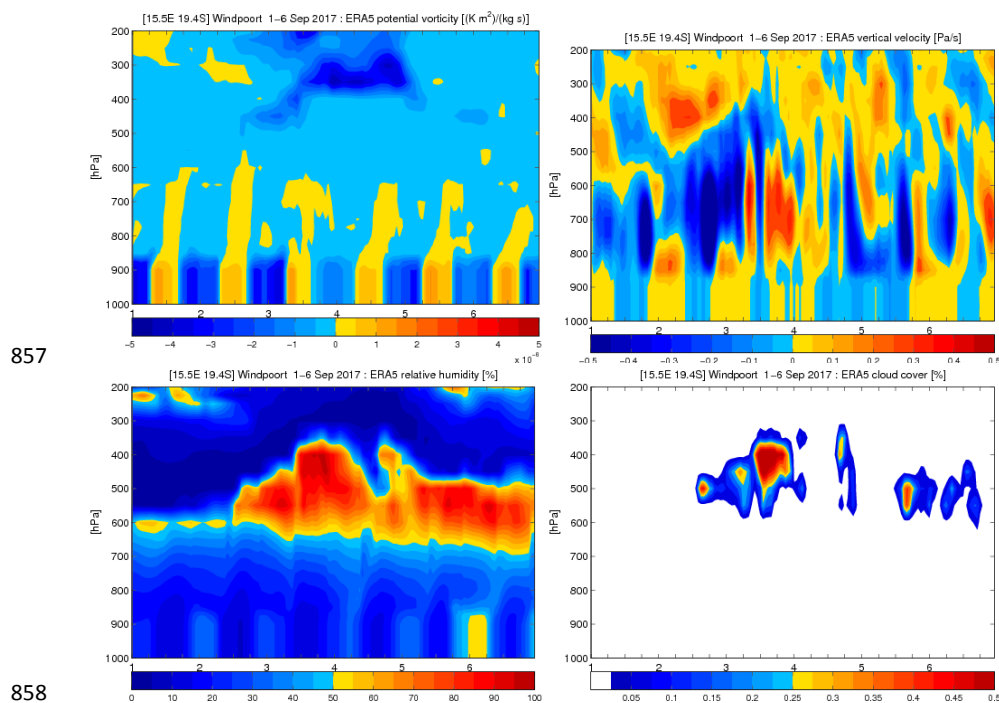


Figure 12: As in Figure 10, but ending at 1200 UTC 6 September 2017 for the F09 flight track.

856



859 **Figure 13.** Time-height cross-section of (a) potential vorticity ($\text{K m}^2 \text{kg}^{-1} \text{s}^{-1}$), (b) vertical velocity (Pa s^{-1}),
860 (c) relative humidity (%) and (d) cloud cover over Windpoort between 1 and 6 September 2017 from
861 hourly ERA 5 reanalysis. Ascending motions are associated with negative ω values.

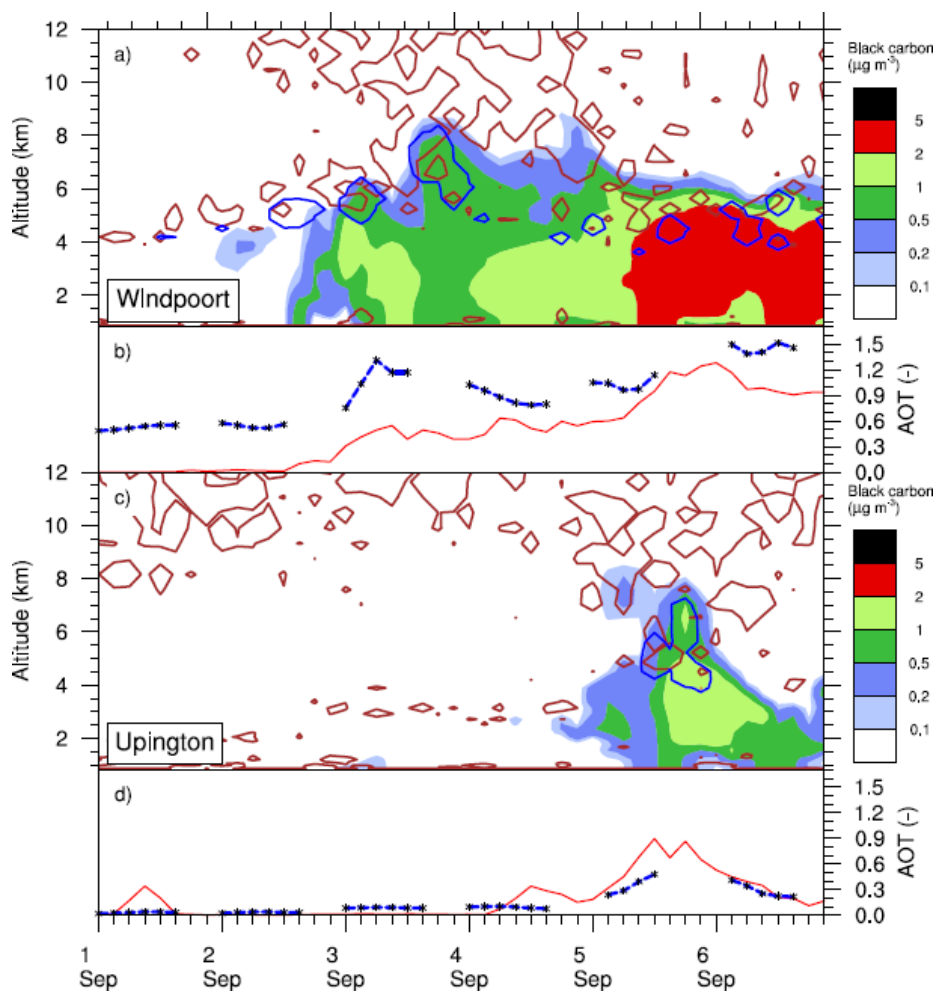


Figure 14: (a) Top panel: time height evolution of black carbon tracer concentration (colour) between 1 and 6 September 2017 from the Meso-NH simulation over Windpoort. Blue contours represent liquid water while brown contours represent potential vorticity. Bottom panel: AOT derived from Meso-NH (solid line, BBA only) and sun-photometer (blue crosses). (b) Same as (a), but for Uppington.

862

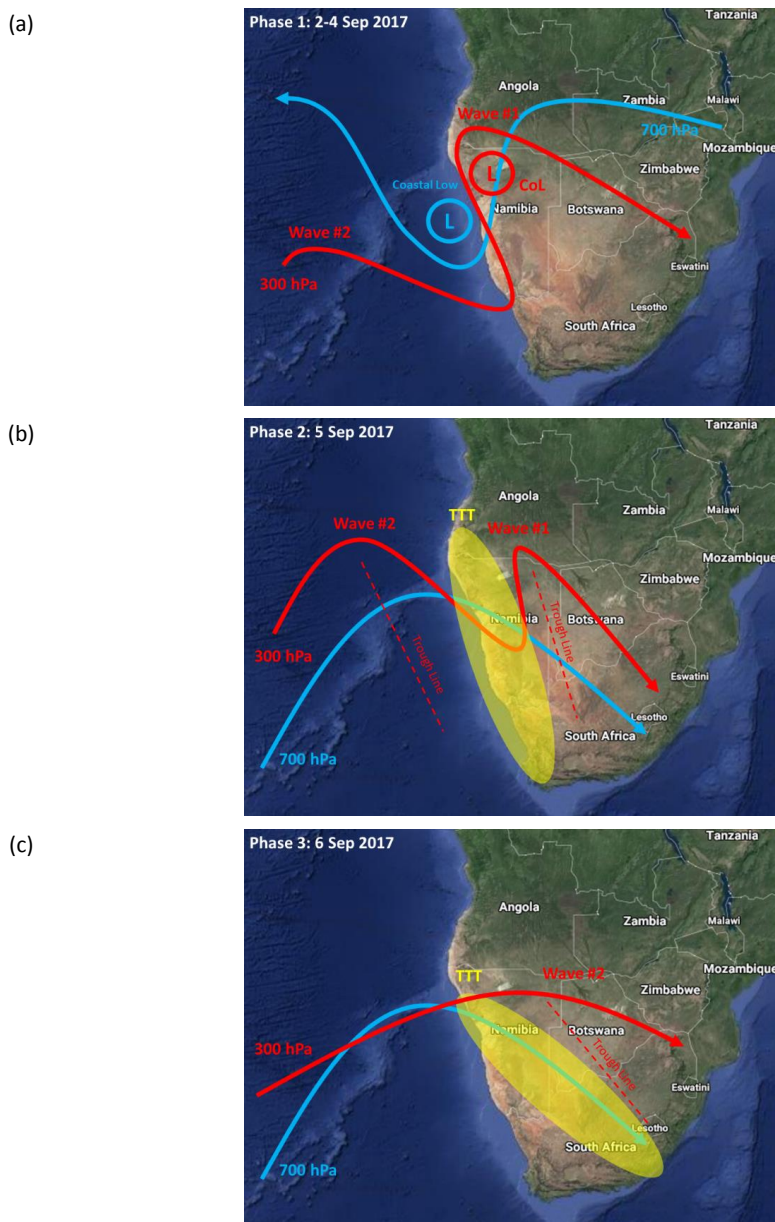


Figure 15: Map of southern Africa with the main dynamical features described in the text during the period 2-6 September 2017. (a) Phase 1 (2-4 September) with the easterly flow at 700 hPa (blue line with arrow) and the imbedded coastal low (blue L), together with the westerly waves at 300 hPa (red line with arrow) and the imbedded CoL (red L). (b) Phase 2 (5 September) with the location of the 2 westerly waves and associated trough lines (red dashed lines), the westerly mid-level flow at 700 hPa (blue line with arrow) and the location of the formed TTT (yellow shaded area). (c) Phase 3 (6 September) with the passage of the 2nd westerly wave and the associated trough line over the continent and the eastward displacement of the TTT. Map credit: © Google Earth 2021.